EMBRY-RIDDLE
Aeronautical University
SCHOLARLY COMMONS

Dissertations and Theses

12-2016

Effect of Flow-Acoustic Resonant Interactions on Aerodynamic Response of Transitional Airfoils

Joseph Hayden

Follow this and additional works at: https://commons.erau.edu/edt

 Part of the Aerodynamics and Fluid Mechanics Commons

Scholarly Commons Citation

Hayden, Joseph, "Effect of Flow-Acoustic Resonant Interactions on Aerodynamic Response of Transitional Airfoils" (2016). *Dissertations and Theses*. 302.
https://commons.erau.edu/edt/302

This Thesis - Open Access is brought to you for free and open access by Scholarly Commons. It has been accepted for inclusion in Dissertations and Theses by an authorized administrator of Scholarly Commons. For more information, please contact commons@erau.edu.

EFFECT OF FLOW-ACOUSTIC RESONANT INTERACTIONS ON AERODYNAMIC RESPONSE OF TRANSITIONAL AIRFOILS

A Thesis

Submitted to the Faculty

of

Embry-Riddle Aeronautical University

by

Joseph Hayden

In Partial Fulfillment of the

Requirements for the Degree

of

Master of Science in Aerospace Engineering

December 2016

Embry-Riddle Aeronautical University

Daytona Beach, Florida

EFFECT OF FLOW-ACOUSTIC RESONANT INTERACTIONS ON AERODYNAMIC RESPONSE OF TRANSITIONAL AIRFOILS

by

Joseph Hayden

A Thesis prepared under the direction of the candidate's committee chairman, Dr. Vladimir Golubev, Department of Aerospace Engineering, and has been approved by the members of the thesis committee. It was submitted to the School of Graduate Studies and Research and was accepted in partial fulfillment of the requirements for the degree of Master of Science in Aerospace Engineering.

THESIS COMMITTEE

Chairman, Dr. Vladimir Golubev

Member, Dr. Mankbadi

Member, Dr. Gudmundsson

Department Chair, Dr. Anastasios Lyrintzis
or Graduate Program Coordinator, Dr. Madgy Attia

12.8.2016
Date

Dean of College of Engineering, Dr. Maj Mirmirani

12/8/2016
Date

Vice Chancellor, Academic Support, Dr. Christopher Grant

12/9/16
Date

TABLE OF CONTENTS

LIST OF TABLES

LIST OF FIGURES

SYMBOLS

ρ	Density
p	Pressure
T	Temperature
u	Tangential Velocity
v	Normal Velocity
w	Spanwise Velocity
φ	Flux component
L	Turbulent Length
τ	Time Scale
k	Wave Number
ω	Frequency
I	Turbulence Intensity
α	Angle of Attack
c	Chord Length
U	Freestream Velocity

ABBREVIATIONS

AFL	Acoustic Feedback Loop
dB	Decibel
L	Lift
D	Drag
Re	Reynolds Number
M	Mach Number
ILES	Implicit Large Eddy Simulation
RFG	Random Flow Generation
AoA	Angle of Attack
Hz	Hertz
RMS	Root Mean Squared
C_L	Lift Coefficient
C_D	Drag Coefficient
FFT	Fast Fourier Transform
T-S	Tollmien-Schlichting
K-H	Kelvin-Helmholtz
C_f	Skin Friction Coefficient
C_p	Pressure Coefficient
DNS	Direct Numerical Simulation

ABSTRACT

Hayden, Joseph MSAE, Embry-Riddle Aeronautical University, December 2016. Effect of Flow-Acoustic Resonant Interactions on Aerodynamic Response of Transitional Airfoils.

A high-accuracy numerical study is conducted to examine the impact of flow-acoustic resonant interactions on the aerodynamic response of symmetric and cambered airfoils in the realistic transitional flow regimes with Re_c=140,000 and M=0.0465 as well as the low Reynolds number flow regime with Re_c=10,000 and M=0.2. The symmetric NACA-0012 and the cambered SD7003 airfoils are investigated at various angles of attack that have been found previously to include both the tone and no-tone producing regimes, with specific focus on the aerodynamic lift response. Additional simulations are conducted with a low-intensity synthetic turbulence introduced upstream of the airfoils in order to trip the boundary layer on the airfoil surface and thus eliminate the acoustic feedback loop as the tone-generating mechanism. The current work focuses on comparing the lift, drag, and lift to drag ratio curves in the uniform vs. turbulent flow cases to determine the impact of the acoustic feedback loop on the airfoil aerodynamic performance for both realistic and low Reynolds number flow conditions.

1. Introduction

1.1. Motivation

Airfoil noise produced by an acoustic feedback loop (AFL) is an effect found in the transitional flow regimes. This flow regime includes the operating conditions used by most small scale aircraft and drones incorporating various civilian and military applications from remote controlled recreational planes to surveillance drones. For both of these applications, noise is a great concern, either for public consideration or stealth applications. Because the discrete tones produced by the AFL can be as high as 40 dB's (Nash et al., 1999) above background noise, the presence of an AFL can provide a massive setback in noise reduction efforts. However, it was recently proposed by Dr. Ikeda et al., (2014) of the Japan Aerospace Exploration Agency (JAXA) that the presence of these tones can also be responsible for increased aerodynamic performance, correlating in increases to both Lift and Drag with a net increase in the Lift to Drag ratio. The research presented was done at the flow regime of Mach number 0.2 and Reynolds Number of 10,000. Because this flow regime is at such a low Reynolds number and high velocity given that Reynolds, it is a predominantly unrealistic flow regime. For instance, calculating for an airfoil at sea level the chord length would be just 2.13 millimeters. This makes the flow very difficult to simulate and impossible to replicate in a wind tunnel. Therefore, the findings in Ikeda et al., (2014) could not be validated against a similar experiment and the results performed at a higher Reynolds number did not observe the same aerodynamic effect as the simulations. Because of this, it was decided that a flow regime more consistent with real world applications should be tested to determine if this effect is also found there as well as replicating the simulations presented in order to

duplicate results.

1.2. Airfoil Noise

Noise is classified in one of two ways. Either broadband noise, which is a combination of multiple frequencies all around the same level or decibel, or a discrete tone. Noise generated by airfoils is often broadband noise. It is created when the vortices that develop along the boundary layer during the transition from laminar flow to turbulent flow on the pressure and suction side of the airfoil are shed from the trailing edge of the airfoil. As these vortices are shed, the pressure waves scatter generating sound waves. Often this noise is insignificant to the overall noise of the aircraft where the majority of the aircraft noise is attributed to the engine. However, under certain flight conditions it is possible for an acoustic feedback loop to develop, making airfoil noise a more prominent concern for aircraft designers. An acoustic feedback loop is a self-exciting tone where the pressure waves at the trailing edge travel back upstream and interact with the vortices in the boundary layer to create higher pressure tones. Tones generated due to an AFL have the same frequency as the vortex shedding at the trailing edge of the airfoil. In order for an AFL to develop, there must be a laminar separation bubble in phase with the vortex generation on the suction side of the airfoil.

1.3. Ikeda Results

This research topic originated due to the paper “Unsteady Aerodyanmic Characteristics of Cambered Four-digit NACA Airfoils at Low Reynolds Number” by Ikeda et al,. (2014). The purpose of this paper was to test a variety of four-digit NACA airfoils between 0 and 10 degrees AoA in increments of 1 degree at a Mach Number of

0.2 using 2-D numerical simulations and investigate the aerodynamic response. All airfoils tested had a thickness of 6% chord length but varied in maximum camber height and camber location. This paper shows that during this flow regime the aerodynamic response can change drastically depending on the presence of an AFL. The Figure below shows a Lift coefficient vs. AoA plot taken from this paper, there is a very clear jump in Lift coefficient in the higher angles of attack for all airfoils shown. The location when the jump occurs is dependent on airfoil configuration with no clear trend for predictability but there is consistency across all the airfoils tested.

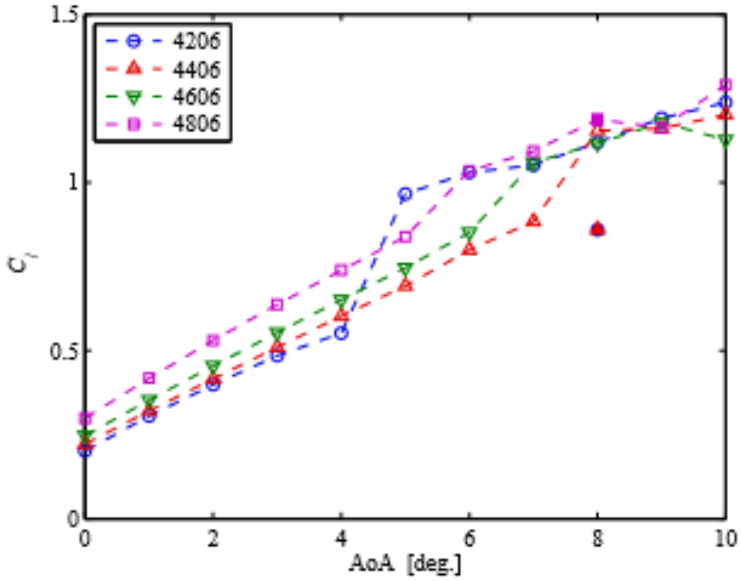

Figure 1.1 Time-averaged lift curves of 2-D simulation results for NACA-4x06 airfoils (Ikeda et al., 2014)
Filled markers denote 3-D simulation results at 8 degree AoA

The cause of this jump is considered to be the presence of the AFL corresponding to a shift in the separation bubble toward the leading edge. Wind-Tunnel experiments were attempted to recreate the simulation results. However, due to the size of the original simulation, exact reproduction could not be done and larger models were used. With this setup, results were not reproducible in wind-tunnel tests.

1.4. Objective of Current Work

While the results shown by Ikeda are very promising, there are also questions left unanswered. Throughout the paper there was no effort to compare the results to simulations without the AFL. No attempt was made to eliminate the AFL and provide a direct comparison of aerodynamic response.

The purpose of this paper is to research the effect of the AFL on aerodynamic performance further. This research will focus around the NACA-0012 and SD7003 airfoils. The NACA-0012 is widely used as a benchmark airfoil with extensive studies available for comparison while the SD7003 is a cambered airfoil used to examine the effect of geometry on the results. These airfoils will be subjected to two different flow regimes and various angles of attack. The first objective of these tests is to determine where the AFL is produced. Then, an upstream turbulence method will be introduced to the flow. This has been shown to trip the boundary-layer causing early transition to turbulence and successfully eliminating the AFL (Golubev et al,. 2014). This will allow for direct comparison of the aerodynamic performance under identical flow conditions. This will allow us to determine if the AFL is the cause of the lift increase or if this increase is due to other, unrelated interactions.

2. Numerical Models

In this work, two numerical codes are used. The first is an ILES code that provides the flow field. The flow field produced by the ILES code provides the pressure coefficients along the airfoil surface necessary to calculate the acoustic data as well as the aerodynamic data as well as flow separation regions and time-averaged flow data. The second code is an upstream turbulence model implemented into the ILES code that provides the "trip" to the boundary layer necessary to eliminate the AFL. The codes are discussed below.

2.1. The ILES Code

For these simulations, the FDL3DI code developed by Visbal and Gaitonde of the AFRL is used. FDL3DI is a robust, well validated, high-accuracy compressible Navier-Stokes solver. This code uses a 6^{th}-order Pade-type compact differencing spatial discretization developed by Lele (1992) coupled with 8^{th}-order low-pass filters. The time-marching is achieved using a 2^{nd}-order implicit approximately-factored method of Beam and Warming (1978) which is augmented with Newton-like subiterations.

The full Navier-Stokes are cast in strong conservative form after transforming from a Cartesian coordinate system to a general time-dependent curvilinear coordinate system $(x, y, z, t) \rightarrow (\xi, \eta, \zeta, \tau)$. The Navier-Stokes equations is then represented in vector notation in terms of nondimensional variables as

$$\frac{\partial}{\partial \tau}\left(\frac{\vec{U}}{J}\right) + \frac{\partial \hat{F}}{\partial \xi} + \frac{\partial \hat{G}}{\partial \eta} + \frac{\partial \hat{H}}{\partial \zeta} = \frac{1}{Re}\left[\frac{\partial \hat{F}_v}{\partial \xi} + \frac{\partial \hat{G}_v}{\partial \eta} + \frac{\partial \hat{H}_v}{\partial \zeta}\right] \tag{2.1}$$

Where $\vec{U} = \{\rho, \rho u, \rho v, \rho w, \rho E\}$ denotes the solution vector and $J = \partial(\xi, \eta, \zeta, \tau) / \partial(x, y, z, t)$ is the transformation Jacobian. The inviscid fluxes $\hat{F}, \hat{G}$ and $\hat{H}$ discussed in Anderson

(1984) are

$$\hat{F} = \begin{bmatrix} \rho\hat{U} \\ \rho u\hat{U} + \hat{\xi}_x p \\ \rho v\hat{U} + \hat{\xi}_y p \\ \rho w\hat{U} + \hat{\xi}_z p \\ (\rho E + p)\hat{U} - \hat{\xi}_t p \end{bmatrix} \tag{2.2.1}$$

$$\hat{G} = \begin{bmatrix} \rho\hat{V} \\ \rho u\hat{V} + \hat{\eta}_x p \\ \rho v\hat{V} + \hat{\eta}_y p \\ \rho w\hat{V} + \hat{\eta}_z p \\ (\rho E + p)\hat{V} - \hat{\eta}_t p \end{bmatrix} \tag{2.2.2}$$

$$\hat{H} = \begin{bmatrix} \rho\hat{W} \\ \rho u\hat{W} + \hat{\zeta}_x p \\ \rho v\hat{W} + \hat{\zeta}_y p \\ \rho w\hat{W} + \hat{\zeta}_z p \\ (\rho E + p)\hat{W} - \hat{\zeta}_t p \end{bmatrix} \tag{2.2.3}$$

Where

$$\hat{U} = \hat{\xi}_t + \hat{\xi}_x u + \hat{\xi}_y v + \hat{\xi}_z w \tag{2.3.1}$$

$$\hat{V} = \hat{\eta}_t + \hat{\eta}_x u + \hat{\eta}_y v + \hat{\eta}_z w \tag{2.3.2}$$

$$\hat{W} = \hat{\zeta}_t + \hat{\zeta}_x u + \hat{\zeta}_y v + \hat{\zeta}_z w \tag{2.3.3}$$

$$E = \frac{T}{(\gamma - 1)M_\infty^2} + \frac{1}{2}(u^2 + v^2 + w^2) \tag{2.4}$$

Here, $\hat{\xi}_x = J^{-1}\ \partial\xi/\partial x$ with similar definitions for the other metric quantities. The Cartesian velocity components are represented with *u, v,* and *w.* The density is shown as ρ, p for pressure, and T for temperature. The perfect gas relationship $p = \rho T/\gamma M^2_\infty$ is assumed. All flow variables have been normalized by their freestream values except for pressure, which has been nondimensionalized by $\rho_\infty u_\infty^2$.

The 6th-order compact scheme requires the solution of a tridiagonal system. In this example, ϕ, can represent any metric such as a flux component or flow variable.

$$\alpha\phi'_{i-1} + \phi'_i + \alpha\phi'_{i+1} = b\frac{\phi_{i+2} - \phi_{i-2}}{4\Delta\xi} + a\frac{\phi_{i+1} - \phi_{i-1}}{2\Delta\xi} \tag{2.5}$$

Where α = 1/3, a = 11/9, and b = 1/9.

Compact-difference discretizations are nondissipative, leading to numerical instabilities due to the growth of high-frequency modes stemming from mesh nonuniformity and nonlinear flow conditions. In order to counteract this inherent flaw found in many centered differencing schemes, a high-order implicit filtering technique is incorporated. The solution vector ϕ, is filtered through the following tridiagonal system, with the filtered solution vector represented by $\hat{\phi}$.

$$\alpha_f\hat{\phi}_{i-1} + \hat{\phi}_i + \alpha_f\hat{\phi}_{i+1} = \sum_{n=0}^{F}\frac{a_n}{2}(\phi_{i+n} - \phi_{i-n}) \tag{2.6}$$

The adjustable parameter α_f must satisfy the inequality $-0.5 < \alpha_f \leq 0.5$, with higher adjustable parameter values corresponding to a less dissipative filter. For poor quality meshes, a value around 0.1 is recommended. For higher quality meshes, values ranging between 0.3 and 0.5 are more appropriate, for these simulations, a value of 0.4 was used. The filter is typically chosen to be two orders of accuracy higher than the differencing scheme, as mentioned previously, for the 6th-order differencing scheme used, the 8th-order low-pass filter was used.

The FDL3DI code has explicit as well as implicit time-marching schemes available. However, for applications such as aeroacoustics that require extremely fine resolution, the stability constraints of the explicit 4th-order Runge-Kutta scheme was found to be too restrictive and inefficient. Therefore, the implicit, approximately-factored

method of Beam and Warming (1978) was chosen. This method is augmented through the use of Newton-like subiterations in order to achieve 2nd-order time accuracy. This allows for errors due to linearization, diagonalization, and explicit boundary conditions to be eliminated. Typically three subiterations are applied for each time step. This method also includes nonlinear artificial dissipation terms to enhance stability. These terms include both 2nd and 4th-order dissipation operators scaled by the spectral radius.

2.2. The Turbulence Model

The current study implements a random flow generation model (RFG) discussed by Golubev et al. (2011) where an upstream turbulent flow field is created using a three-dimensional Fourier spectrum for perturbation flow velocity which matches prescribed energy spectrum with given turbulence integral scales. As described by Kraichnan (1970) and expanded by Smirnov et al. (2001) the procedure to generate a synthetic turbulent field matching Gaussian spectral distribution involves several steps. The first step is to determine the orthogonal transformation tensor a_{ij} that will diagonalize the given anisotropic velocity correlation tensor r_{ij} for the turbulent flow velocity field $\{u_i(x_j, t)\}_{i,j=1\ldots3}$.

$$a_{mi}a_{nj}r_{ij} = \delta_{mn}c_{(n)}^2$$

$$a_{ik}a_{kj} = \delta_{ij} \tag{2.7}$$

The scaling coefficients $c_{(n)}$ represent the three turbulent fluctuating velocity components in the coordinate system produced by the transformation tensor a_{ij}. Next, an intermediate randomly fluctuating velocity is constructed using the equations

$$v_i(\tilde{x}_j,\tilde{t}) = \sqrt{\frac{2}{N}}\sum_{n=1}^{N}\left[p_i^n\cos\left(\tilde{k}_j^n\tilde{x}_j - \omega_n\tilde{t}\right) + q_i^n\sin\left(\tilde{k}_j^n\tilde{x}_j - \omega_n\tilde{t}\right)\right] \tag{2.8}$$

Where

$$\tilde{x}_j = \frac{x_j}{L}, \quad \tilde{t} = \frac{t}{\tau}, \quad \tilde{k}_j^n = k_j^n\frac{|c|}{c_j}$$

$$p_i^n = \varepsilon_{ijm}\zeta_j^n k_m^n, \quad q_i^n = \varepsilon_{ijm}\xi_j^n k_m^n$$

$$\zeta_j^n, \xi_j^n, \omega_n \in N(0,1), \quad k_j^n \in N(0,1/2)$$

L and τ represent the turbulent length and time scales found by using the turbulence kinetic energy and dissipation rate from RANS simulations or from an experiment Batten et al., (2004). Random fluctuations are introduced using the permutation tensor ε_{ijm} and $N(M,\sigma)$ represents the normal distribution with M and σ representing the mean and standard deviation respectively. Therefore, a sample Gaussian turbulent energy spectrum is created with wave number k_j^n and frequency ω_n.

$$E(k_j^n) = 16\left(\frac{2}{\pi}\right)^{1/2}(k_j^n)^2\exp(-2(k_j^n)^2) \tag{2.9}$$

Lastly, the constructed fluctuating velocity is rescaled to obtain the required flowfield,

$$w_i(\tilde{x}_j,\tilde{t}) = c_i v_i(\tilde{x}_j,\tilde{t}) \tag{2.10}$$

$$u_i(x_j,t) = a_{ik}w_k(\tilde{x}_j,\tilde{t}) \tag{2.11}$$

As shown by Smirnov et al. (2001), this approach produces the velocity field which is divergence-free for homogeneous turbulence and virtually divergence free for inhomogeneous ones. In order to match the time and space scales of the numerical code, additional rescaling must be implemented.

In the numerical implementation of RFG model discussed in detail in Golubev et al., (2011) and Golubev et al., (2012) the objective is to generate a 3D, incompressible

convected perturbation velocity field. The following equation implements a momentum source to the flowfield developed in the equation above. Using the Fourier transform containing superposition of harmonic functions,

$$u_i(x_j, t) = \sum_{n=1}^{N} \left[a_i^n \cos\left(k_j^n x_j - \omega_n t\right) + b_i^n \sin\left(k_j^n x_j - \omega_n t\right) \right] \tag{2.12}$$

Without loss of generality, the synthesized unsteady disturbance field is considered convected by a uniform mean flow u_∞aligned with the $x_1$direction so that the modal perturbation frequency ω_n is related to the wavenumber k_1^n by $\omega_n = u_\infty k_j^n$. Furthermore, the disturbance is assumed to be incompressible (divergence-free) which implies the following coupling between the modal amplitudes and wavenumbers

$$a_j^n k_j^n = b_j^n k_j^n = 0 \tag{2.13}$$

Interactions between the perturbation modes and other waves are considered negligible. Therefore, the momentum source terms S_i generating the disturbance velocity field in u equation above should satisfy the following relationships

$$\frac{\partial u_i}{\partial t} + U_\infty \frac{\partial u_i}{\partial x_1} = S_i \tag{2.14}$$

It can be shown that the solution for the momentum source terms imposed in the computational domain region with extent Δ_s in the mean flow convection direction (x_1) may be obtained in the form

$$S_i(x_j, t) = \left\{ \begin{array}{ll} \sum_{n=1}^{\infty} \omega_n K_n g(x_1) (b_i^n \sin(\sigma_n) - a_i^n \cos(\sigma_n) & for\ i = 1 \\ \sum_{n=1}^{\infty} U_\infty K_n g'(x_1) (b_i^n \cos(\sigma_n) + a_i^n \sin(\sigma_n) & for\ i = 2, 3 \end{array} \right\} \tag{2.15}$$

Where K_n is the constant

$$K_n = \frac{\left(\frac{k_1^n}{2\pi}\Delta_s\right)^2 - 1}{\sin\left(\frac{k_1^n}{2}\Delta_s\right)} \tag{2.16}$$

And $g(x_1)$is the limiter function defined as

$$g(x_1) = \begin{cases} \frac{1}{2}\left(1 + \cos\left[\frac{2\pi}{\Delta_s}(x_1 - x_{1s})\right]\right) & for\ |x_1 - x_{1s}| \le \frac{\Delta_s}{2} \\ 0 & for\ |x_1 - x_{1s}| > \frac{\Delta_s}{2} \end{cases} \tag{2.17}$$

$g'(x_1) = \ dg/dx_1$, and $\sigma_n = \omega_n t - k_1^n x_{1s} - k_2^n x_2 - k_3^n x_3$. The momentum source terms are thus specified in an upstream region centered at $x_1 = x_{1s}$.

In the numerical procedure, for the synthesized field generated downstream of the source region, the energy spectra $E_i(x_j, f)$ corresponding to the disturbance velocity field are obtained with frequency resolution $\Delta f = 1/T$ and $f_{max} = 1/2\,\Delta t$ based on data samples recorded with period *T* and sampling rate Δt.

3. Results

The objective of the current work is to determine if the presence of the AFL does effect the aerodynamic performance of an airfoil. With the results from Ikeda et al., (2014) showing an impact at the low Re flow regime, the first regime investigated was the M=0.0465 Re_c=140,000. The first object was to determine which AoAs observed the AFL effect. This was done using the ILES code to determine the time-dependent flow field using grids of 1281x789 and 1283x789 for the NACA-0012 and SD7003 respectively matching grid parameters used for high-resolution LES simulations according to Wagner et al., (2007) and are finer compared to the mesh employed in a similar DNS study by Desquesnes et al., (2007). Steady state was reached first by running the code for 600,000 iterations at a time step of 9e-5 corresponding to 54 non-dimensional time cycles or 0.405 and 0.0939 seconds in physical time for the Re_c=140,000 and Re_c=10,000 flow regimes respectively. With steady state achieved data acquisition took place for an additional 750,000 iterations saving flow data every 44 iterations in order to acquire 2^{14} data points allowing for accurate spectra analysis up to 4,000 Hz. Both the NACA-0012 and the SD7003 were tested at a range of AoAs and the surface pressure spectra results were extracted and investigated. The cases with the AFL were noted but all cases were tested again under upstream turbulent flow at an intensity of 7% of the mean flow (I=0.07) to observe if any aerodynamic effects were observed. The pressure spectra results were then compared to determine if the turbulence successfully eliminated the discrete tones produced by the AFL. With successful elimination of the AFL confirmed, the aerodynamic performance was compared. Further boundary-layer statistics were also investigated in order to further understand and

validate results.

3.1. NACA-0012: Mach 0.0465 Re 140,000

3.1.1. Pressure Spectra and Aerodynamic Performance

The effects of the tonal noise on the aerodynamic response is first investigated for a symmetric NACA-0012 airfoil, for several angles of attack (AoAs), with a fixed Re_c=140,000 (corresponding to a flow velocity of U=16m/s). As presented in Table 3.1, the airfoil is installed between 0-10 degrees, which has been previously shown[3] to subject the airfoil to both the tone and no-tone generating regimes. For simplicity, the current work will only focus on three tone generating regime, 0-4 degree AoA. As illustrated in Figure 3.1, the airfoil exhibits a distinct tone in the surface pressure spectra (blue) when in the presence of a uniform upstream flow, indicating the existence of the AFL. However, in order to investigate the effect of the AFL on aerodynamics, the AFL must be eliminated. As suggested in Nguyen et al., (2014), introducing a low-intensity turbulence (*I=0.07,* corresponding to the perturbation RMS velocity of 7 percent of the freestream velocity) in the upstream flow condition would decorrelate the modes associated with the AFL and thus disrupt the feedback loop mechanism. Results shown in Figure 3.1 reveal that the injection of low intensity turbulence upstream of the airfoil does lead to the disruption of the AFL, thus reducing the surface pressure spectra (magenta) to mainly a broadband hump.

Table 3.1 Geometric angle of attack investigated for NACA-0012 Re=140,000 Representative cases (Bold).

Cases	AOA (degree)	Velocity (m/s)
Uniform	**0, 2, 4,** 6, 8, 10	**16**
Turbulent	**0, 2, 4,** 6, 8, 10	**16**

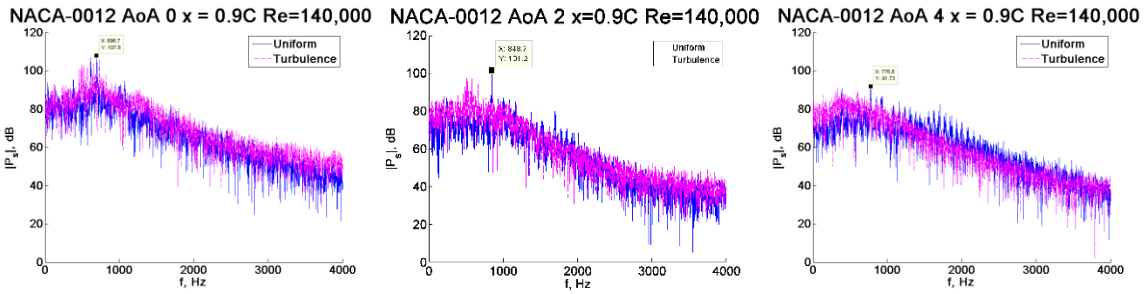

(a) (b) (c)

Figure 3.1 Surface Pressure Spectra Comparison of NACA-0012 Uniform (blue) and Turbulent (magenta) Cases. a) 0 º AoA, b) 2 º AoA, c) 4 º AoA.

To ensure the aerodynamic response of the airfoil is not altered by the upstream turbulence, Figure 3.2 compares the coefficient of lift time history for the 3 representative cases. The variation in C_L over the time shows no significant deviation between the uniform and turbulence cases, aside from the higher amplitude fluctuations in the turbulent-flow cases with AoA=2 and 4 degrees. To supplement the surface spectra in Figure 3.1 and reveal the existence/suppression of tones, the lift time histories are processed using FFT to obtain the lift spectra, as shown in Figure 3.3. The results show that the turbulent upstream cases induce scattering in the lower frequency range while the uniform cases are dominated by a single peak frequency. It should be noted that the scattering associated with turbulence is indicative of the suppression of tones which usually appear as a single peak frequency seen in the results obtained for the uniform upstream flow.

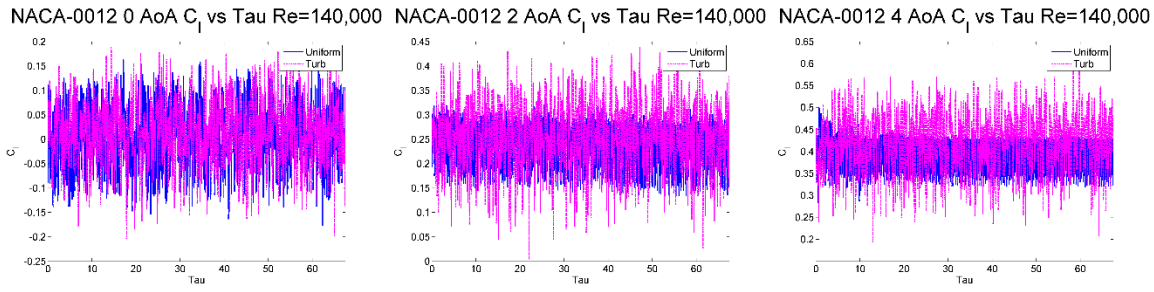

(a) (b) (c)

Figure 3.2 Coefficient of Lift vs. Non-Dimensional Time Comparison for NACA-0012 Uniform (blue) and Turbulent (magenta) Cases. a) 0 º AoA, b) 2 º AoA, c) 4 º AoA.

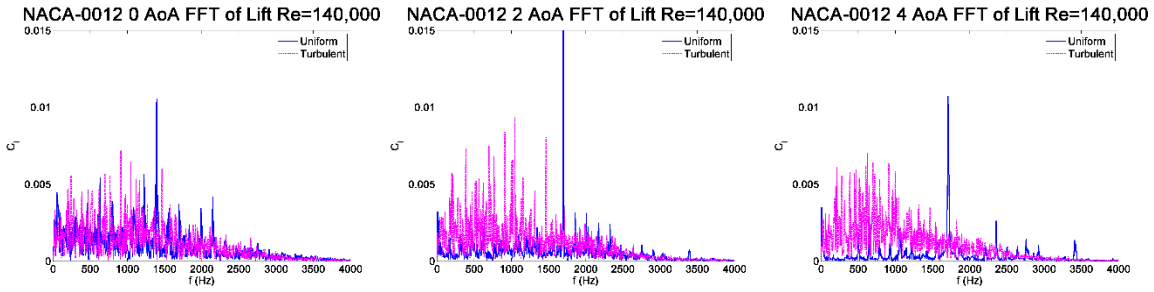

(a) (b) (c)

Figure 3.3 Comparison of Fast Fourier Transform of Lift for NACA-0012 Uniform (blue) and Turbulent (magenta) Cases. a) 0 º AoA, b) 2 º AoA, c) 4 º AoA.

The aerodynamic performance of the NACA-0012 was investigated by comparing the time-average lift and drag coefficients, as well as the lift to drag ratio for uniform and turbulent cases across the tested AoAs. Both the lift and drag coefficients (Figures 3.4 and 3.5) show a consistent trend with no significant differences between the uniform and turbulent cases apart from minor deviations. The lift results were also compared against the theoretical sectional lift coefficient for the inviscid flat plate $(2\pi\alpha)$ and wind tunnel experiment results at Re_c=160,000 from Sheldahl (1981), to validate the numerical simulations and confirm the known impact of the viscous effects. The numerical results show a very good agreement with the flat-plate prediction and wind tunnel results at low AoA; however, as AoA increases, the viscous effects present in the simulations cause the trend to diverge for both the simulation and the wind tunnel results. The drag coefficient results were compared against wind tunnel tests. The results show a significant

overestimation of the drag coefficient as AoA increases. It is expected that a 2D simulation will over predict the drag values compared to 3D simulations as well as wind tunnel results. The overall aerodynamic performance of the NACA-0012 was tested by comparing the lift to drag ratio for the uniform and turbulent conditions in Figure 3.6. The comparison shows good agreement for most AoAs tested with the largest deviations observed at 2 and 4 degrees AoA. These deviations correspond to the lift gap observed at the same angles in Figure 3.4. It is also observed that the peak lift to drag ratio occurs at low AoA due to typical results, this is attributed to the unnaturally high drag coefficient observed by 2D simulations at high AoAs. The agreement among both C_L and C_D for the uniform and turbulent cases is essential in revealing the fact that the existence of the AFL does not affect the aerodynamic response of a symmetric NACA-0012 in any significant manner in the realistic transitional flow condition.

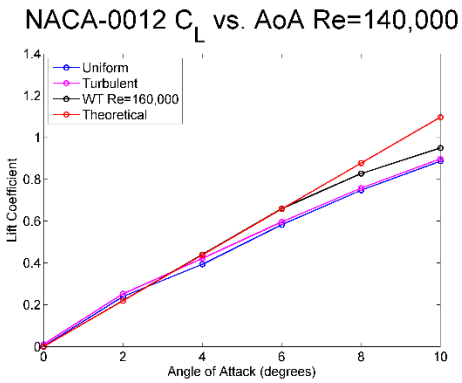

Figure 3.4 Time-averaged C_L vs. Angle of Attack Comparison for NACA-0012 Uniform (blue), Turbulent (magenta) Cases, Wind Tunnel Re=160,000 (black), Inviscid Flat-Plate (red).

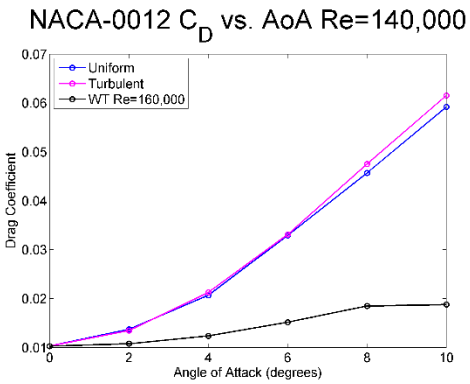

Figure 3.5 Time-averaged C_D vs. Angle of Attack Comparison for NACA-0012 Uniform (blue), Turbulent (magenta) Cases, Wind Tunnel Re=160,000 (black).

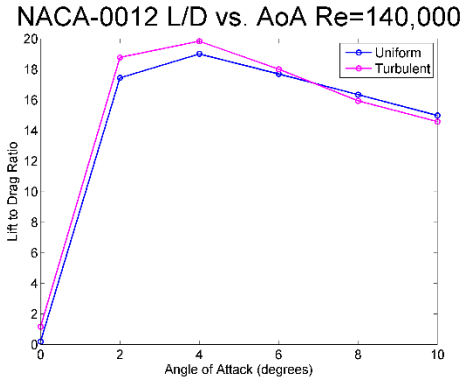

Figure 3.6 Lift to Drag Ratio vs. Angle of Attack for NACA-0012 Uniform (blue) and Turbulent (magenta) Cases.

3.1.2. Boundary Layer Statistics

To better understand the discrepancies between the current results and the conclusions of Ikeda et al. (2014), various boundary-layer statistical data are investigated to study the differences for the tone- and no-tone generating regimes. Figure 3.7 illustrates the instantaneous z-vorticity plots for each representative case revealing a significant change in the boundary-layer dynamics when turbulence is introduced. The plots show instabilities to occur earlier along the airfoil surface due to the impinging turbulence modes in Eqn. (2.12) through the phase-locking mechanism previously shown in Nguyen et al., (2014).

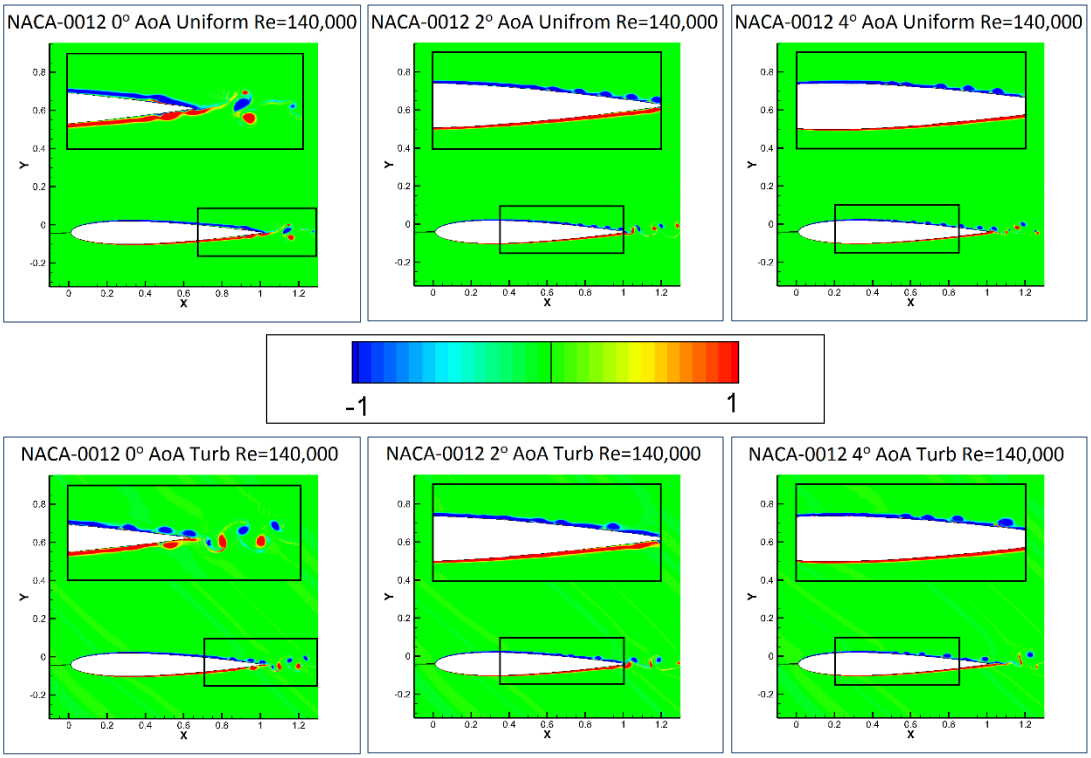

Figure 3.7 Instantaneous Z-Vorticity Contours for NACA-0012
Top) Uniform, Bottom) Turbulent Cases. Left) 0° AoA, Middle) 2 ° AoA, Right) 4 ° AoA.

Time-averaged U-Velocity contours in Figure 3.8 further confirms the effect of turbulence on the boundary layer dynamics. The difference between the uniform and turbulent upstream flow condition is quite evident based on the fact that the thin separation regions occurring in the uniform cases are not present in the turbulence cases. In the absence of turbulence, these separation regions induce disturbances in the boundary layer resulting in a switch from the slowly growing Tollmien-Schlichting (T-S) waves to the fast-growing Kelvin-Helmholtz (K-H) waves to trigger and sustain the AFL. The location and existence of these regions are clearly shown in the uniform-case (blue) mean pressure distributions in Figure 3.9 in the form of a hump on the suction side. In the cases with turbulence, the hump does not exist, thus resulting in the suppression of the feedback loop. In addition, the pressure distribution surrounding the airfoil surface shows no significant differences between the uniform and turbulent cases indicating that the

aerodynamic response is similar, as suggested in Figure 3.4.

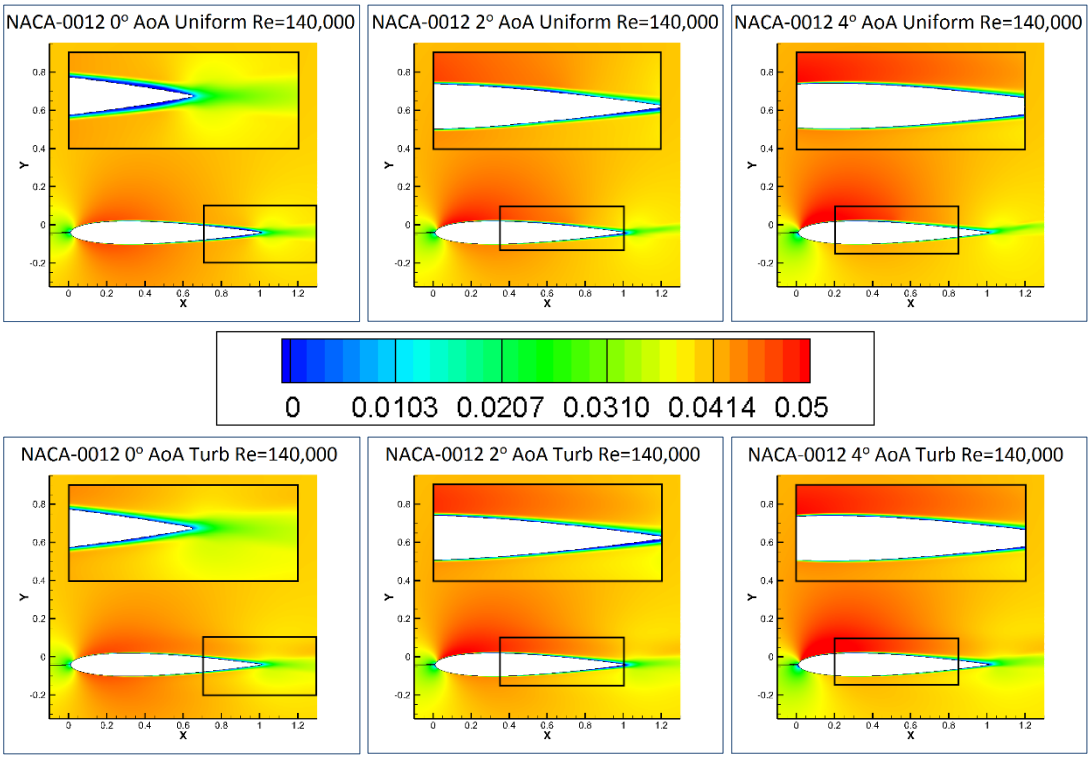

Figure 3.8 Time-averaged U-Velocity Contours NACA-0012
Top) Uniform, Bottom) Turbulent Cases. Left) 0º AoA, Middle) 2 º AoA, Right) 4 º AoA.

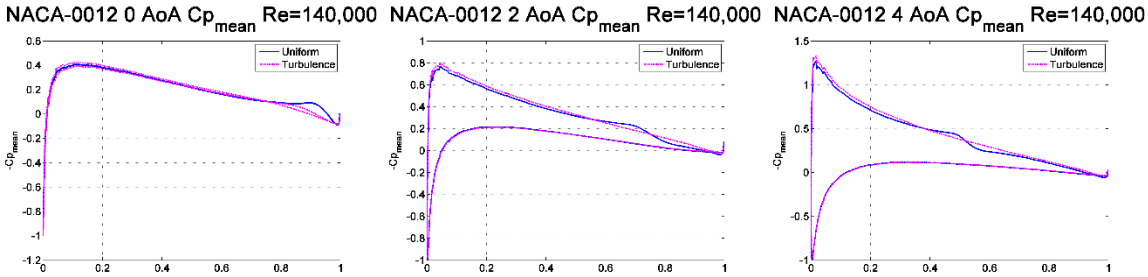

(a) (b) (c)

Figure 3.9 Mean Pressure Coefficient Comparison for NACA-0012
Uniform (blue) and Turbulent (magenta) Cases. a) 0 º AoA, b) 2 º AoA, c) 4 º AoA.

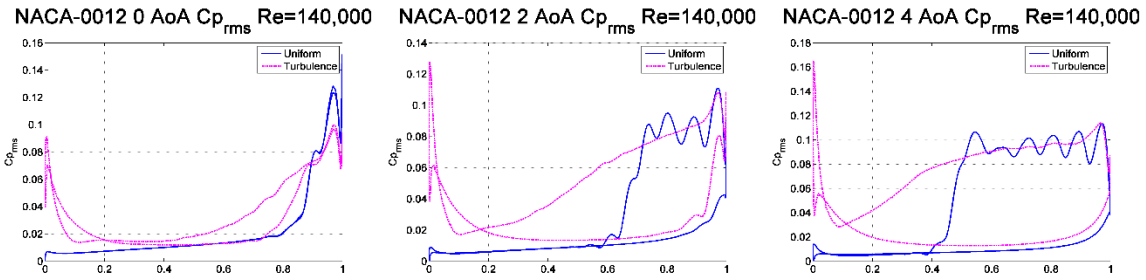

(a) (b) (c)

Figure 3.10 RMS Pressure Coefficient Comparison for NACA-0012 Uniform (blue) and Turbulent (magenta) Cases. a) 0 ^{o} AoA, b) 2 ^{o} AoA, c) 4 ^{o} AoA.

Figure 3.10 illustrates the RMS pressure distributions on the airfoil surface obtained for the turbulent intensity I=0.07 in comparison with those for the uniform upstream flow case. The differences in RMS pressure are more apparent than for the mean pressure due to the development of strong leading-edge peaks followed by the overall much higher RMS levels on the suction side. Eventually, the RMS levels saturate and a match for all three cases is observed in the aft portion of the airfoil.

Based on the skin friction plot of Figure 3.11, the location of separation and reattachment for each case can be easily obtained and compares well with Figure 3.9. For the uniform case at 0 degree AoA, the region is shown to exist between 0.7c-0.9c and correspond very well with Figures 3.7 and 3.8. In the presence of turbulence, the separation region completely disappears due to transition to the turbulent boundary layer, which thus explains the suppression of the AFL on the suction side and hence the absence of the clearly defined spectral tones in Figures 3.1 and 3.3.

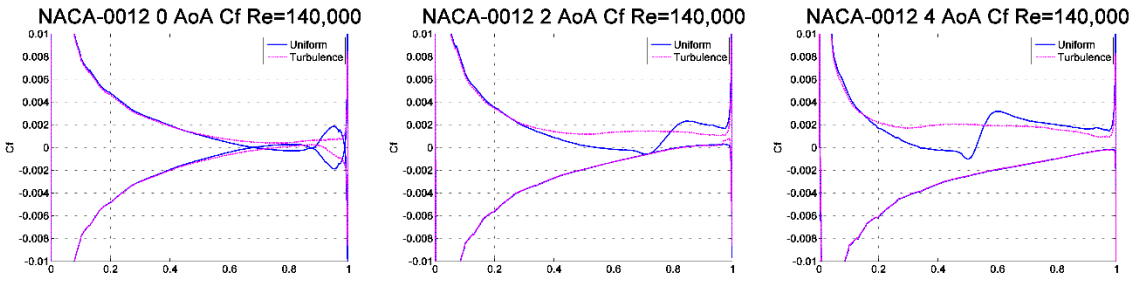

(a) (b) (c)

Figure 3.11 Skin Friction Coefficient Comparison for NACA-0012
Uniform (blue) and Turbulent (magenta) Cases. a) 0 º AoA, b) 2 º AoA, c) 4 º AoA.

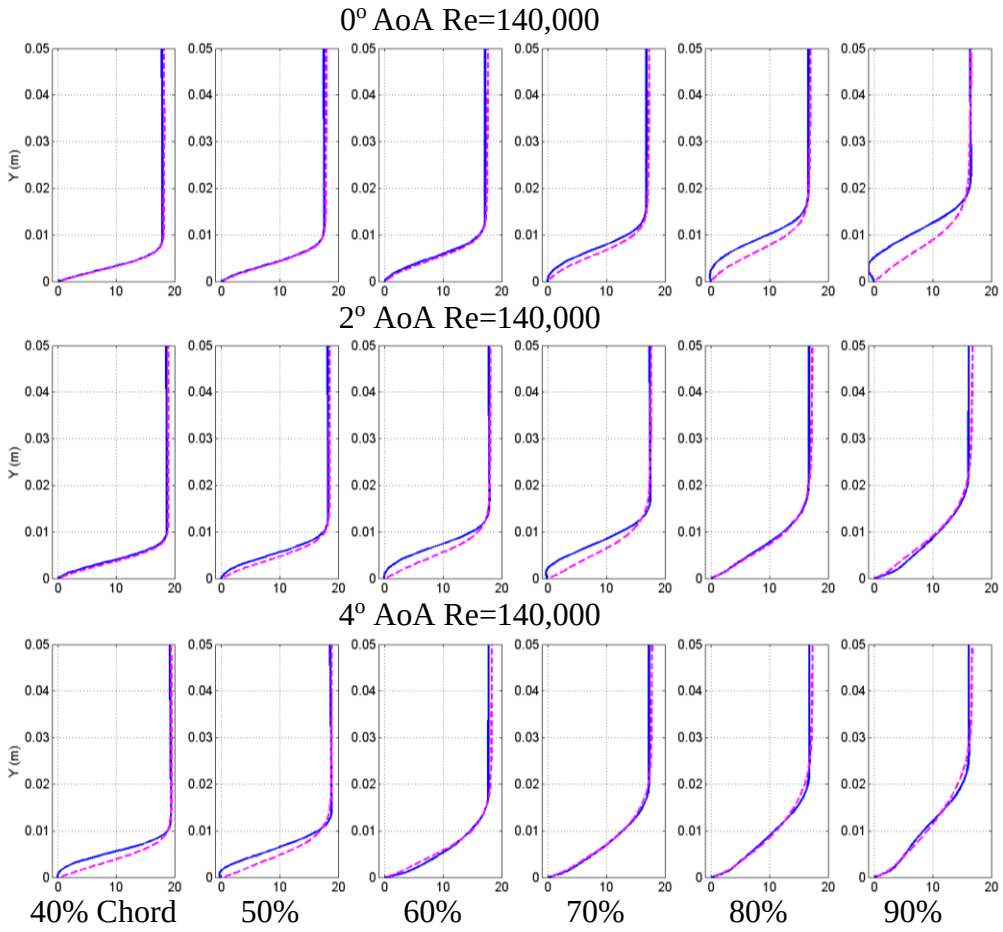

Figure 3.12 U-Velocity Profile Comparison for NACA-0012
Uniform (blue) and Turbulent (magenta) Cases. Top) 0 º, Middle) 2 º, Bottom) 4 º AoA.

U-velocity profiles along the upper surface of the airfoil are compared at various locations in Figure 3.12. Data is obtained from 40 to 90 percent chord in increments of 10 to capture the boundary-layer development for the 3 cases. Interestingly, the differences in U-velocity profiles between uniform and turbulent upstream flow condition is most

prominent in the cases with lower AoA and diminishes as AoA increases. This is a result of the lower AoA cases exhibiting mostly laminar flow across the airfoil surface. As upstream turbulence is added, the flow changes significantly as illustratedd in Figures 3.10 and 3.11 resulting in greater difference in boundary layer dynamics. At higher AoAs, the flow can be assumed to be transitional or near-turbulent, hence adding more turbulence will not trigger severe changes.

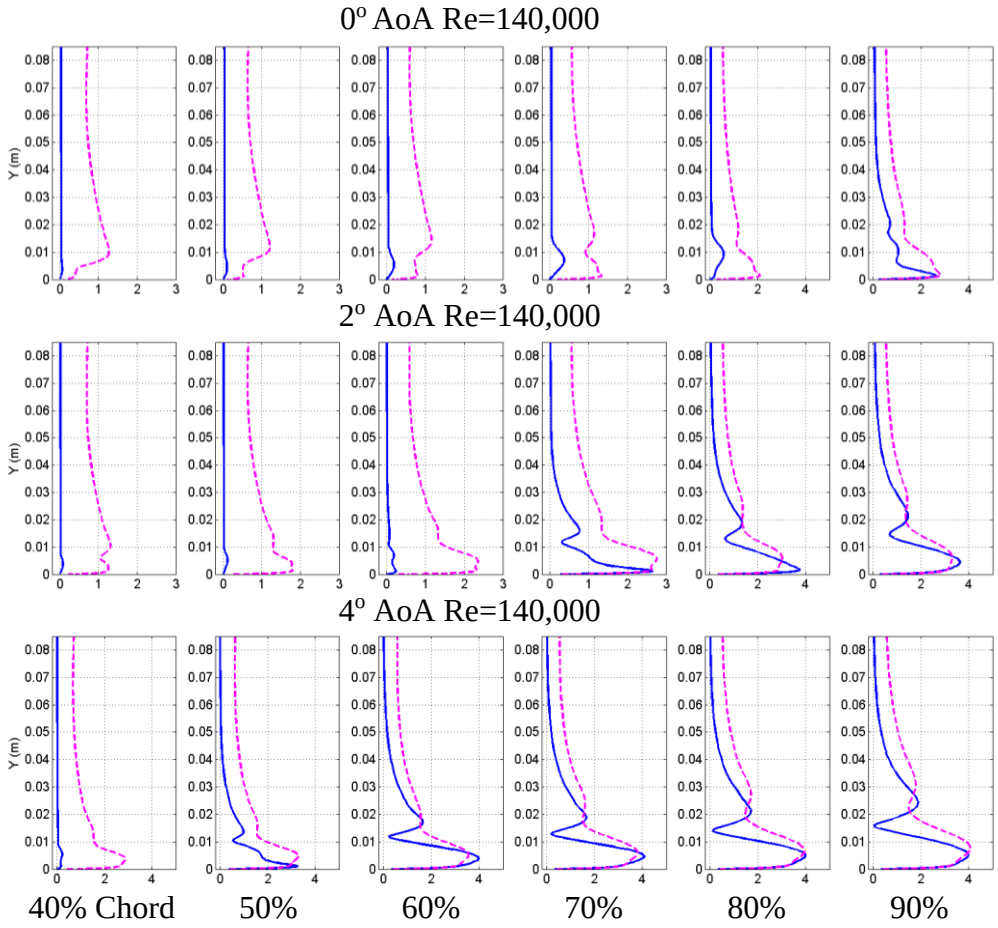

Figure 3.13 RMS of U-Velocity Profile Comparison for NACA-0012
Uniform (blue) and Turbulent (magenta) Cases. Top) 0 °, Middle) 2 °, Bottom) 4 ° AoA.

The U_{rms}-velocity profile plots in Figure 3.13 reveal a similar trend to that of Figure 3.12, with the lower AoA cases showing greater differences between the uniform and turbulent flow cases than for higher AoA case. It may also be noted that the presence

of the upstream turbulence eliminates the inflection point in the boundary-layer velocity profile which presence is indicative of the switch from the viscous T-S to the shear-layer K-H instability waves associated with the formation of a thin separation bubble.

3.2. SD7003: Mach 0.0465 Re 140,000

3.2.1. Pressure Spectra and Aerodynamic Performance

The cambered SD7003 airfoil is examined for AoAs between -4 and 8 degrees (Table 3.2) corresponding to the range recently investigated experimentally by Yakhina et al., (2015) to reveal the transition between the tone- and no-tone producing regimes. Note that the experimental results by Yakhina et al., (2015) suggest that the SD7003 airfoil has a smaller tone-generating envelope when compared to the symmetric NACA-0012 airfoil. The current numerical simulations conducted for the SD7003 airfoil focus on the tone-generating regimes for AoAs between -2 and 2 degrees.

Results of the surface pressure spectra for both the uniform and turbulent cases are shown in Figure 3.13 revealing a successful elimination of the tones produced under uniform flow conditions via turbulent inflow. As shown in the NACA-0012 cases, tripping of the boundary layer is achieved with a turbulence intensity of 7% (*I=0.07)* of the incoming flow velocity.

Table 3.2 Geometric angle of attack investigated for SD7003 Re=140,000
Representative cases (Bold)

Cases	AOA (degree)	Velocity (m/s)
Uniform	-4, **-2, 0, 2,** 4, 6, 8	**16**
Turbulent	-4, **-2, 0, 2,** 4, 6, 8	**16**

Figure 3.14 compares the C_L history for the 3 tone producing cases. Similar to the

symmetric airfoil, the variation in C_L over time shows no significant deviation between uniform and turbulent cases, other than the higher amplitude fluctuations. Lift spectra shown in Figure 3.16 exhibit a trend comparable to that of the NACA-0012 in which the uniform flow spectra is dominated by a single peak while the turbulent cases show many scattering frequencies. These results validate the surface pressure spectra in Figure 3.14 illustrating the presence of a dominant single tone in all 3 uniform cases and a broadband hump for the turbulent cases suggesting the suppression of discrete tones.

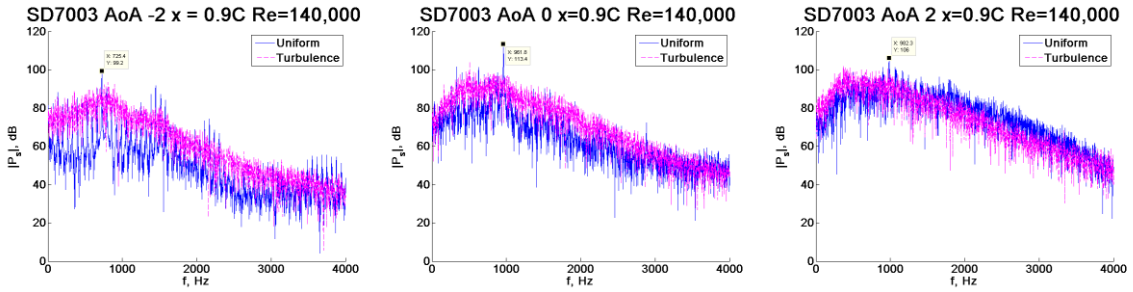

(a) (b) (c)

Figure 3.14 Surface Pressure Spectra Comparison of SD7003 Uniform (blue) and Turbulent (magenta) Cases. a) -2 º AoA, b) 0 º AoA, c) 2 º AoA.

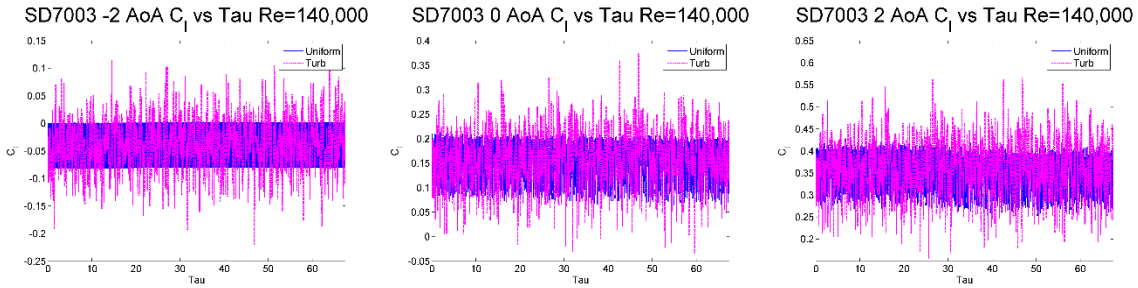

(a) (b) (c)

Figure 3.15 Coefficient of Lift vs. Non-Dimensional Time Comparison for SD7003 Uniform (blue) and Turbulent (magenta) Cases. a) -2 º AoA, b) 0 º AoA, c) 2º AoA.

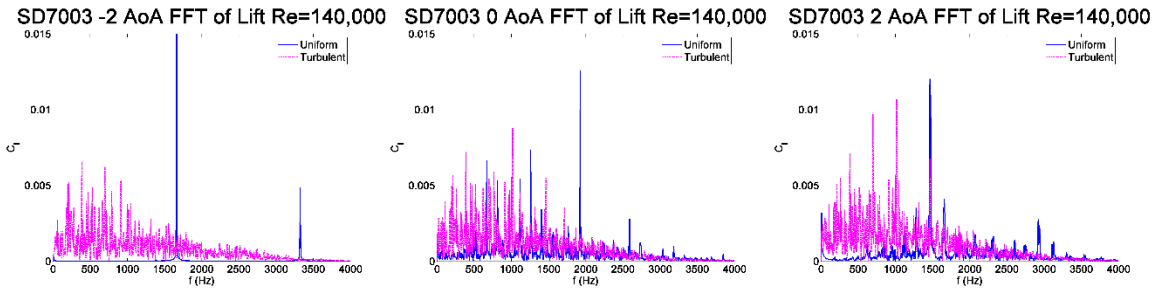

(a) (b) (c)

Figure 3.16 Comparison of Fast Fourier Transforms of Lift for SD7003 Uniform (blue) and Turbulent (magenta) Cases. a) -2 ^{o} AoA, b) 0 ^{o} AoA, c) 2 ^{o} AoA.

The time-averaged C_L shown in Figure 3.17 validates observations from Figure 3.15, proposing that the lift remains consistently close between the uniform and turbulent cases. Aside from a minor discrepancy at -4 degree AoA, the time-averaged lift coefficient shows that the agreement between the uniform and turbulent flow simulations for the SD7003 airfoil is slightly better than for the symmetric NACA-0012 case. Additionally, the results correspond very well to the theoretical inviscid flat-plate predictions (adjusted for the cambered airfoil), wind tunnel analysis performed by Selig et al., (1989), and previous ILES analysis by Galbraith et al., (2010). This observation remains consistent with the drag results shown in Figure 3.18 as well. The drag results between uniform and turbulent simulations show clear agreement throughout the AoAs tested. These results were also compared to wind tunnel experimental data performed by Selig et al., (1989) conducted at Re_c=150,000. As with the NACA-0012 results, the drag is over predicted at high AoAs due to a consistent effect found in 2D simulations. The overall aerodynamic performance comparison (Figure 3.19) further validates the consistency observed in Figures 3.17 and 3.18. The lift to drag ratio is more consistent along all AoAs when compared to the NACA-0012 plots in Figure 3.6. As with the NACA-0012, the SD7003 lift to drag ratios are artificially low due to the over prediction of drag coefficient. As elucidated by the time-averaged lift and drag coefficients, the

aerodynamic response of the cambered SD7003 airfoil appears unaffected by the presence of the AFL.

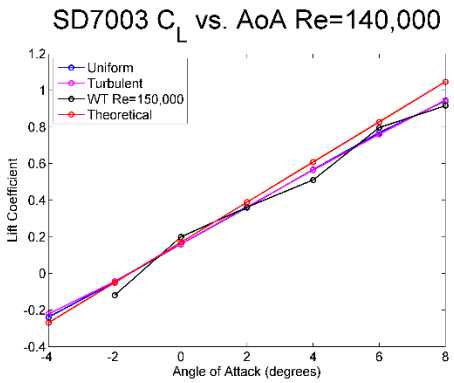

Figure 3.17 Time-averaged C_L vs. Angle of Attack for SD7003 Uniform (blue) and Turbulent (magenta) Cases, Wind Tunnel Re=150,000 (black), Inviscid Flat Plate (red).

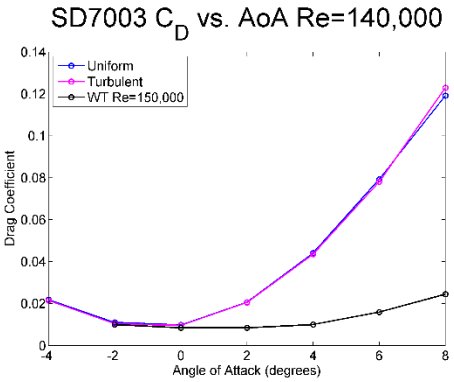

Figure 3.18 Time-averaged C_D vs. Angle of Attack for SD7003 Uniform (blue) and Turbulent (magenta) Cases, Wind Tunnel Re=150,000 (black).

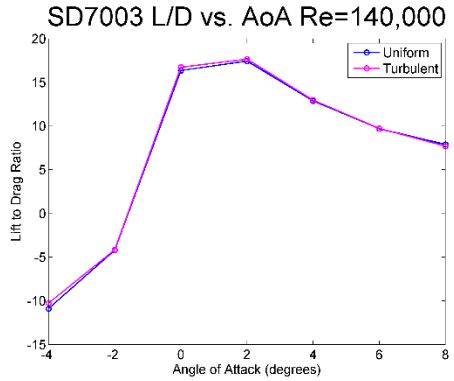

Figure 3.19 Lift to Drag Ratio vs. Angle of Attack for SD7003 Uniform (blue) and Turbulent (magenta) Cases.

3.2.2. Boundary Layer Statistics

Figure 3.20 illustrates the instantaneous z-vorticity revealing the vortex formation and subsequent separation region at each AoA. In addition, results show turbulence to have a greater effect on enhancing the vorticity dynamics along the airfoil surface in comparison with the symmetric NACA-0012 cases. Time-averaged U-Velocity contours (Figure 3.21) are presented to complement the instantaneous z-vorticity contours shown in Figure 3.20. As also exhibited for the symmetric NACA-0012 cases, the thin separation regions for the SD7003 cases are clearly suppressed by the induced turbulence.

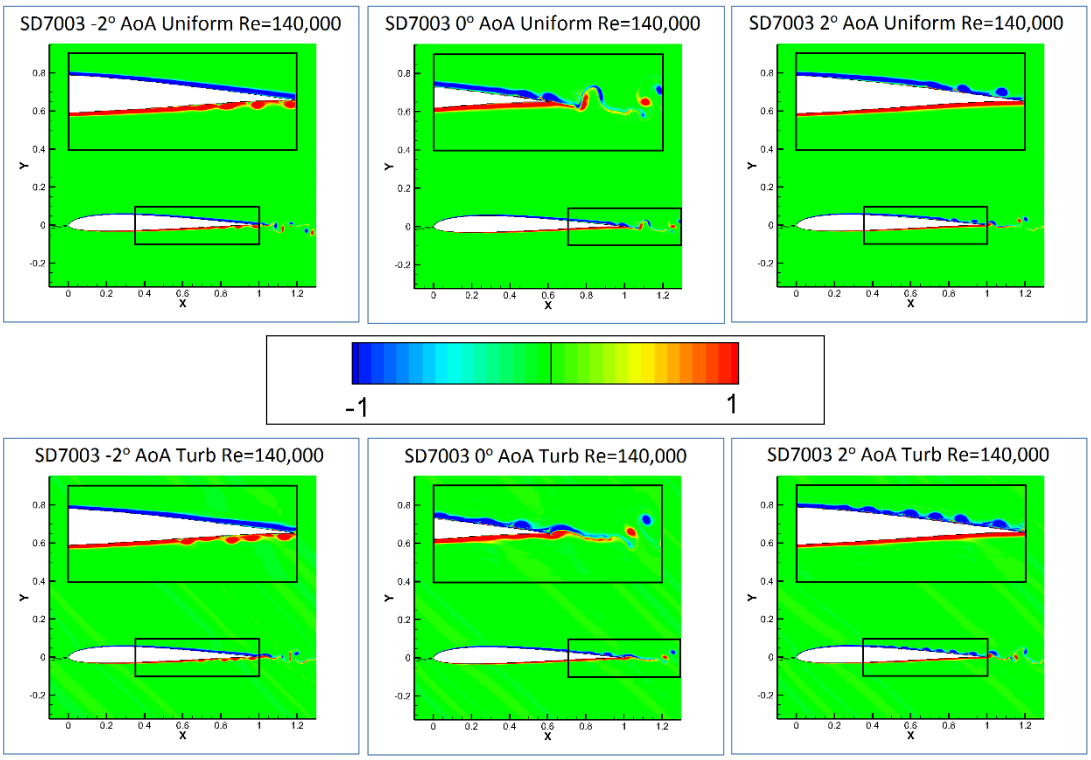

Figure 3.20 Instantaneous Z-Vorticity Contours for SD7003
Top) Uniform, Bottom) Turbulent Cases. Left) -2° AoA, Middle) 0 ° AoA, Right) 2° AoA

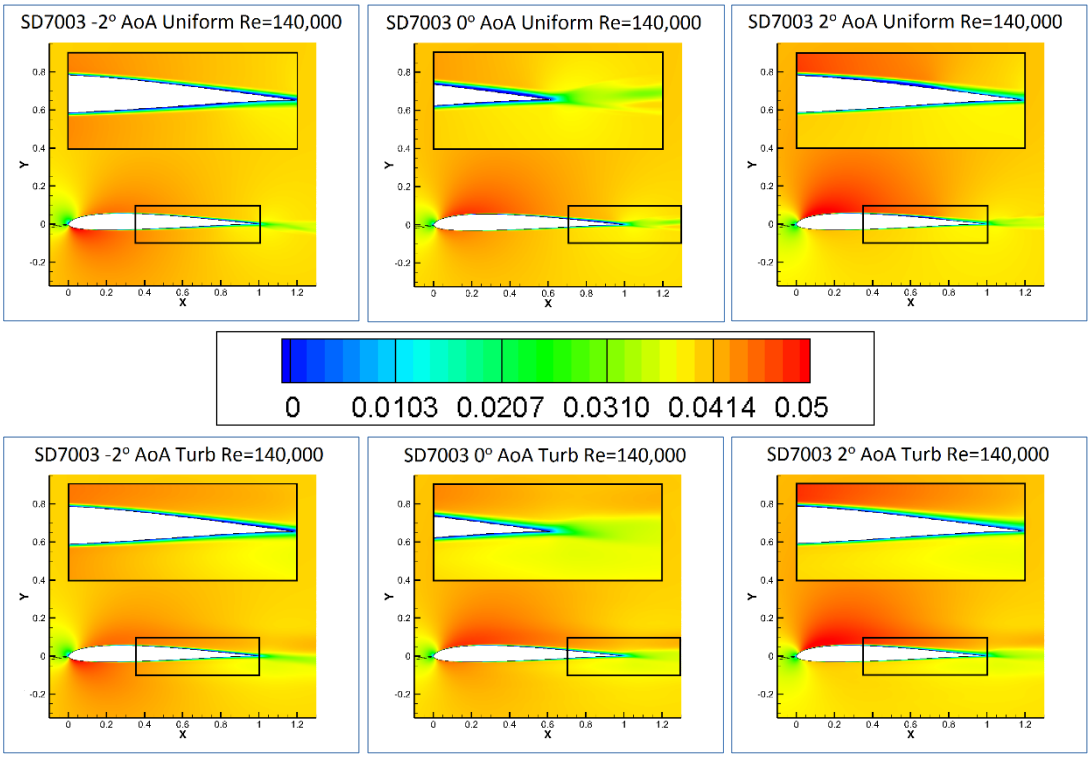

Figure 3.21 Time-averaged U-Velocity Contours SD7003
Top) Uniform, Bottom) Turbulent Cases. Left) -2^{o} AoA, Middle) 0^{o} AoA, Right) 2^{o} AoA

Mean pressure coefficient in Figure 3.22 show similar pressure distribution along the airfoil surface for both the uniform and turbulent upstream conditions, in line with the findings for the NACA-0012. In the case with turbulence, the hump resulting from the thin separation region does not exist, thus resulting in the suppression of the feedback loop. In addition, the pressure distribution surrounding the airfoil surface shows no significant differences between the uniform and turbulent case indicating the aerodynamic response is similar, as suggested in Figure 3.17.

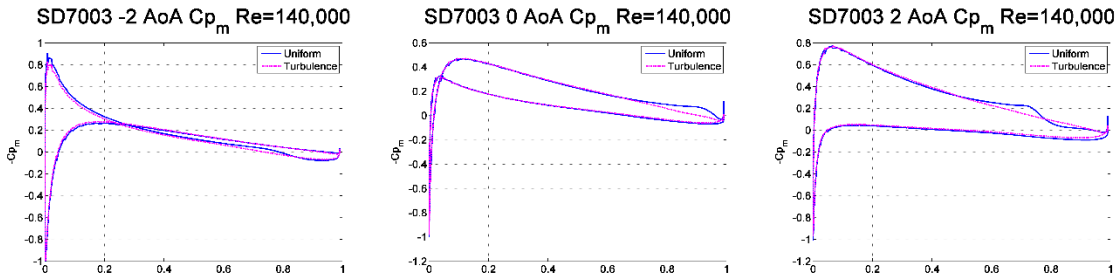

(a) (b) (c)

Figure 3.22 Mean Pressure Coefficient Comparison for SD7003 Uniform (blue) and Turbulent (magenta) Cases. a) -2 ^{o} AoA, b) 0 ^{o} AoA, c) 2 ^{o} AoA.

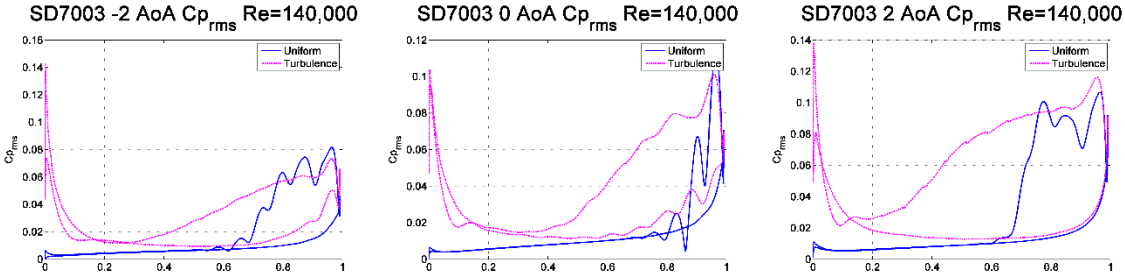

(a) (b) (c)

Figure 3.23 RMS Pressure Coefficient Comparison for SD7003 Uniform (blue) and Turbulent (magenta) Cases. a) -2 ^{o} AoA, b) 0 ^{o} AoA, c) 2 ^{o} AoA.

The RMS pressure distributions shown in Figure 3.23 exhibit similar trends to the results obtained for NACA-0012. In accordance with Figure 3.10, the turbulent case simulation shows the development of strong leading-edge peaks followed by the overall much higher RMS levels on the suction side. Correlating the results in Figures 3.22 and 3.23 reveals the location of the separation region inducing the high RMS fluctuations. Skin friction plots (Figure 3.24) further validates the existence of the separation region in the uniform cases necessary to generate the tone-producing AFL. As was shown for the symmetric NACA-0012 cases, in the presence of the upstream turbulence the airfoil boundary layer transitions to the fully turbulent flow resulting in the disruption of the AFL.

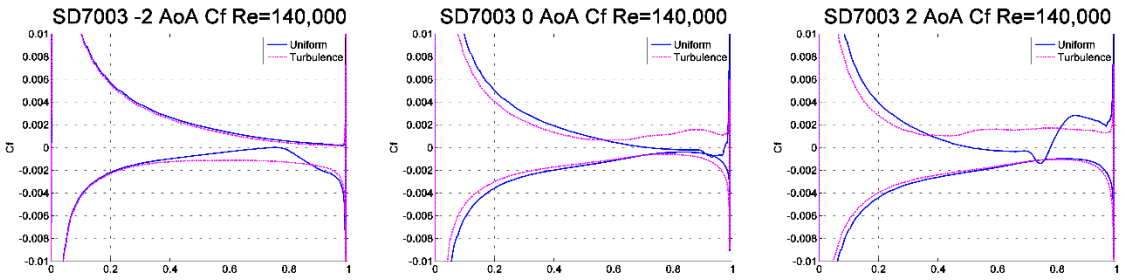

(a) (b) (c)

Figure 3.24 Skin Friction Coefficient Comparison for SD7003
Uniform (blue) and Turbulent (magenta) Cases. a) -2 ^{o} AoA, b) 0 ^{o} AoA, c) 2 ^{o} AoA.

U-Velocity profiles in Figure 3.25 show the dynamics of the airfoil suction side where the AFL is present (bottom surface for -2 degrees and upper surface for 0 and 2 degrees). Due to the closer proximity of the separation regions to the trailing edge for the SD7003 cases, the data is extracted from 70 to 95 percent chord allowing for a more detailed analysis. Overall, the velocity profiles show good agreement between the uniform and turbulent cases, which results in similar aerodynamic performance. Reminiscent of the NACA-0012 cases, the reversed flow sections close to the airfoil surface are eliminated in the turbulent cases as shown in the vorticity plots. To better understand the variations present in the boundary-layer profiles, the U_{rms} velocity profiles are examined for each station. Figure 3.26 shows the RMS plots illustrating a similar trend in profile shape throughout the majority of the sections. It is noticed that results for the 70-85 percent chord stations for the 0 degree case are significantly different. This can be explained with the z-vorticity plot in Figure 3.20, which shows that the flow is still laminar in this section resulting in very low amplitude fluctuations. As the flow approaches the separation point for this AoA, the instabilities increase in a similar trend to the turbulent cases.

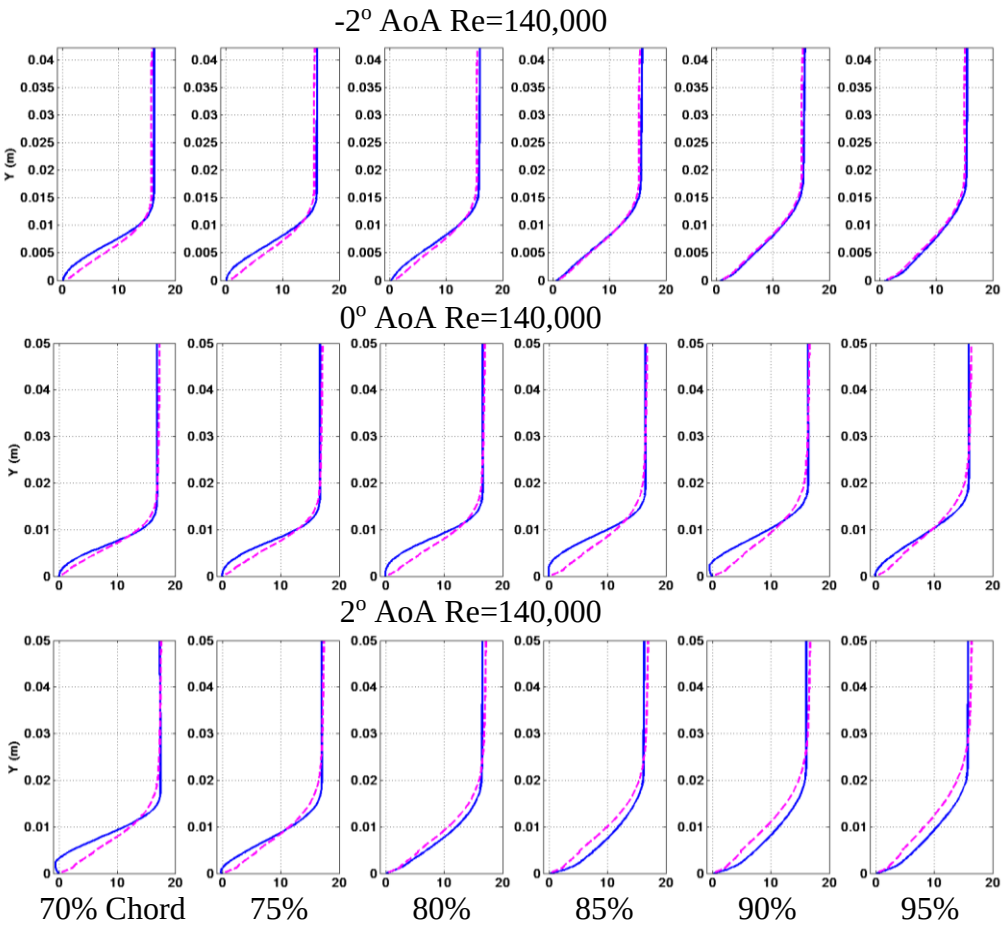

Figure 3.25 U-Velocity Profile Comparison for SD7003
Uniform (blue) and Turbulent (magenta) Cases. Top) -2 º, Middle) 0 º, Bottom) 2 º AoA.

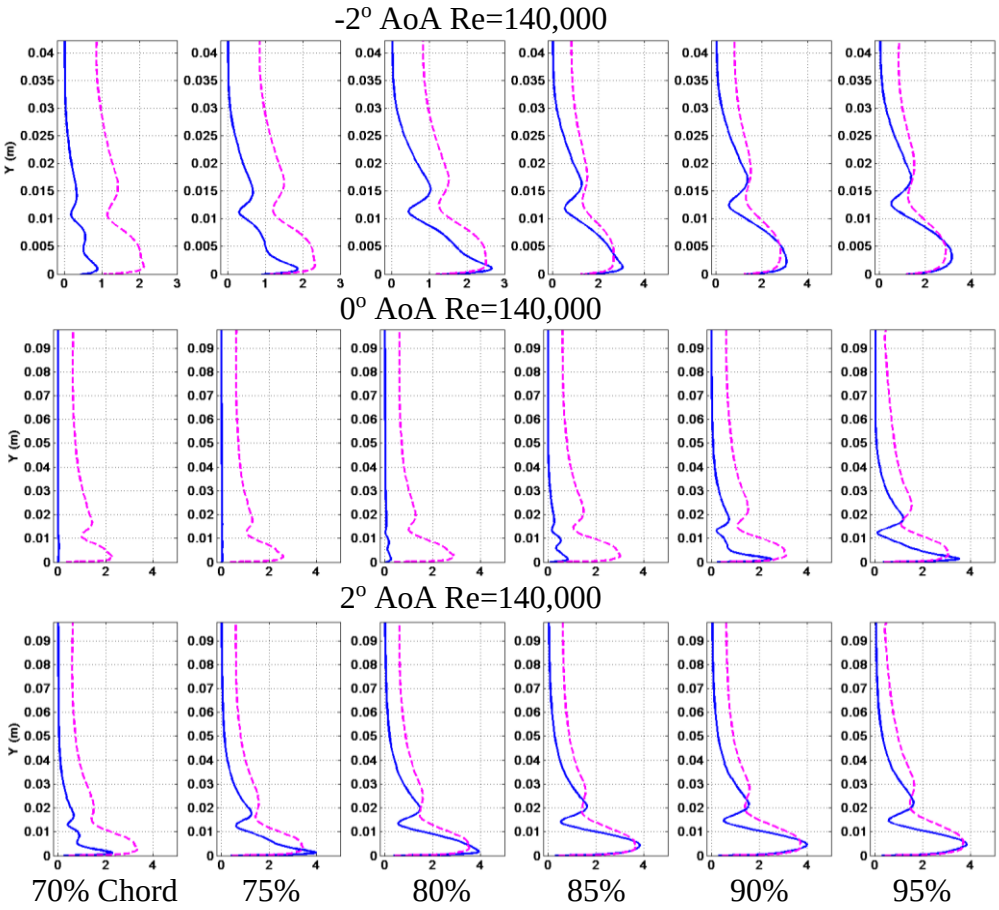

Figure 3.26 U-rms Velocity Profile Comparison for SD7003
Uniform (blue) and Turbulent (magenta) Cases. Top) -2 °, Middle) 0 °, Bottom) 2 ° AoA.

3.3. NACA-0012: Mach 0.2 Re 10,000

It was proposed that the discrepancies found between previous results and Ikeda's findings were due to the inherent differences between the two flow regimes. Because Ikeda's work is done at such a small Reynolds Number the impact of viscous effects will be more apparent and more easily identified. In order to validate this claim, the flow regime used by Ikeda of M=0.2 with a fixed Re_c=10,000 was applied to the NACA-0012 and SD7003 airfoils tested at the same AoAs used in section 3.1 and 3.2 respectively.

3.3.1. Pressure Spectra and Aerodynamic Performance

As in Section 3.1, the NACA-0012 airfoil is tested between 0 and 10 degrees AoA. For this new flow regime the presence of the acoustic feedback loop is found at angles 6 and 8 degrees.

Table 3.3 Geometric angle of attack investigated for NACA-0012 Re=10,000 Representative Cases (Bold)

Cases	AOA (degree)	Velocity (m/s)
Uniform	0, 2, 4, **6, 8,** 10	**69.4**
Turbulent	0, 2, 4, **6, 8,** 10	**69.4**

Figure 3.27 shows the surface pressure spectra for the 6 and 8 degree cases for both uniform and turbulent simulations. The plots show a successful scattering of the discrete tones due to the upstream turbulence implemented. Again turbulence was implemented in order to trip the boundary layer and eliminate the AFL. Due to the increased velocity of this flow regime and the knowledge that the turbulence intensity is dependent on the flow velocity, the necessary turbulence intensity was investigated again in order to determine if a lesser turbulence could be used. It was found that an intensity of 0.8 percent (I=0.008) was again insufficient to eliminate the tones. As before, an intensity of 7 percent (I=0.07) successfully eliminated the discrete tones. This leads to the assumption that the required turbulence intensity is proportionate to the flow velocity and not an independent value.

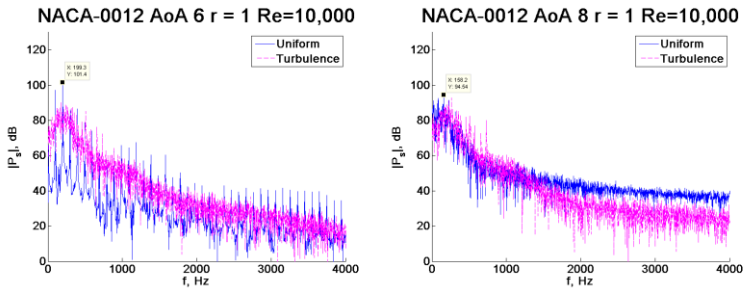

Figure 3.27 Acoustic Spectra Comparison of NACA-0012
Uniform (blue) and Turbulent (magenta) Cases. Left) 6 ^{o} AoA, Right) 8 ^{o} AoA.

The Lift Coefficient over time comparison between the uniform and turbulent cases are shown in Figure 3.28. The plots show that there is a significant disparity between the uniform and turbulent cases for both AoAs shown. In the 6 degree case, the effect of the turbulence is clearly shown. With the AFL suppressed, the lift coefficient is visibly increased. The time-averaged C_L plot in Figure 3.30 shows that a significant transition in lift takes place between 6 and 8 degrees for the uniform case. At this point it is not clear the cause of this transition and the boundary layer statistics discussed later in this section should shed light on the reason for this transition. It was proposed by Ikeda that the presence of the acoustic feedback loop enables earlier flow reattachment along the airfoil surface potentially allowing an increase in lift in flow separation conditions. It is possible that the lift increase is due to the flow reattaching to the airfoil surface but because the AFL is present in cases where lift is both higher and lower than cases with boundary layer tripping, it is difficult to prove whether the AFL is having any effect on the aerodynamic performance. Figure 3.29 shows the Lift spectra for both cases. The Lift spectra validates the results shown in the surface pressure spectra shown in Figure 3.27. Again the tones created by the AFL are successfully scattered by the upstream turbulence.

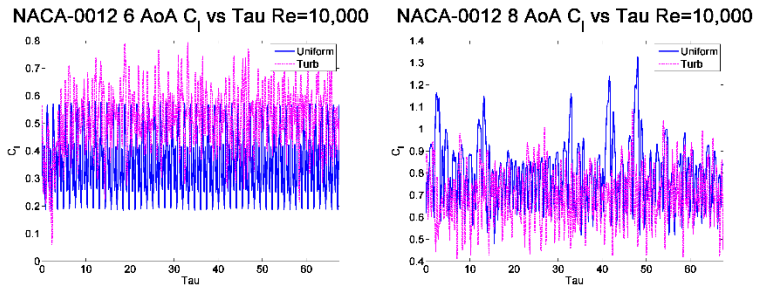

Figure 3.28 Coefficient of Lift vs. Non-Dimensional Time Comparison for NACA-0012 Uniform (blue) and Turbulent (magenta) Cases. Left) 6 º AoA, Right) 8 º AoA.

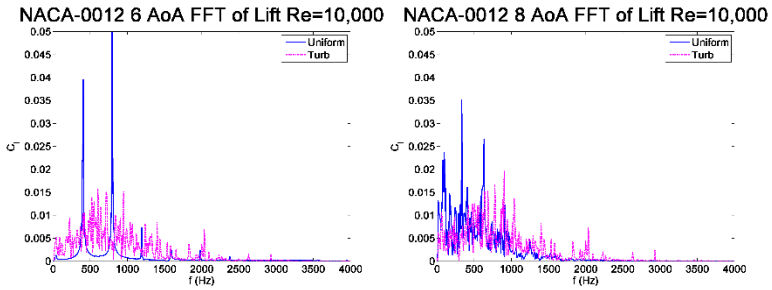

Figure 3.29 Comparison of Fast Fourier Transforms of Lift for NACA-0012 Uniform (blue) and Turbulent (magenta) Cases. Left) 6 º AoA, Right) 8 º AoA.

Figure 3.30 shows significant variation in lift coefficient between the uniform and turbulent cases. The behavior of the uniform results is consistent with the results shown by Ikeda et al., (2014) where a large increase in lift coefficient occurs at higher AoAs. Due to the low Reynolds number and relatively high velocity, flow separation is found to occur even at 0 degrees AoA at this flow regime. It is therefore concluded that the significantly lower lift shown at low AoAs in the uniform flow simulations is in part due to that separation. However, because the turbulent simulations also show significantly reduced lift to the theoretical predictions while achieving improved flow attachment, flow separation is not the only effect reducing the lift. It is expected at such low Reynolds numbers that the viscous effects will play a larger role in the aerodynamic response. This is consistent when comparing these results to Figure 3.4 from Section 3.1. With a higher Reynolds number, the disparity between simulations and theoretical is insignificant at lower AoAs and becomes more apparent the higher the AoA, where flow separation

becomes a greater issue. The lift results are also compared to experimental results performed in a wind tunnel by Sheldahl (1981). The results show that the wind tunnel data follows the general trend of the simulations but does not observe the same transition observered by Ikeda et al., (2014) or the simulations performed for this paper.

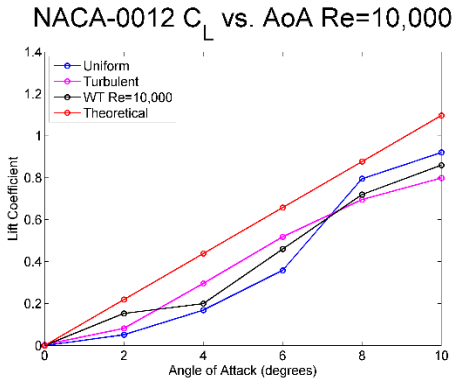

Figure 3.30 Time-averaged C_L vs. Angle of Attack for NACA-0012 Uniform (blue) and Turbulent (magenta) Cases, Wind Tunnel Re=10,000 (black), Inviscid Flat-Plate (red).

The time-averaged drag coefficient is compared in Figure 3.31 against wind tunnel experimental data obtained by Sheldahl (1981) at Re_c=10,000. The plot shows that the uniform simulation shows good correlation against the wind tunnel test data at high AoA and good correlation with the turbulent simulations at low AoA. The turbulent simulations show significant deviation from the uniform simulations. The effect of this increased C_D is compounded with the increased C_L observed in Figure 3.30 when the lift to drag ratio is calculated in Figure 3.32. As discussed in Ikeda et al., (2014), the overall aerodynamic performance does show an increase when comparing the cases with and without the AFL, however, it is difficult to determine the effect of the upstream turbulence. Therefore, the aerodynamic performance does appear to be affected by the presence of the AFL at low Reynolds number flows but the extent of the impact is impossible to determine using this method to eliminate the AFL. The upstream

turbulence disrupts the boundary layer making direct comparison between the tone producing and no tone cases boundary layers meaningless.

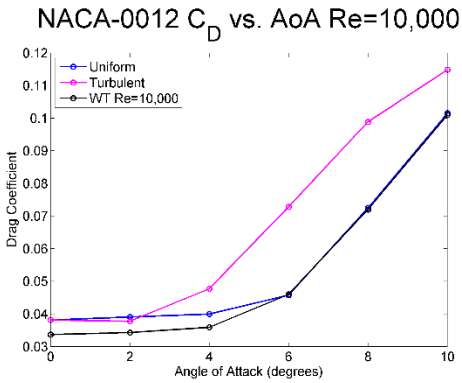

Figure 3.31 Time-averaged C_D vs. Angle of Attack for NACA-0012 Uniform (blue) and Turbulent (magenta) Cases, Wind Tunnel Re=10,000 (black).

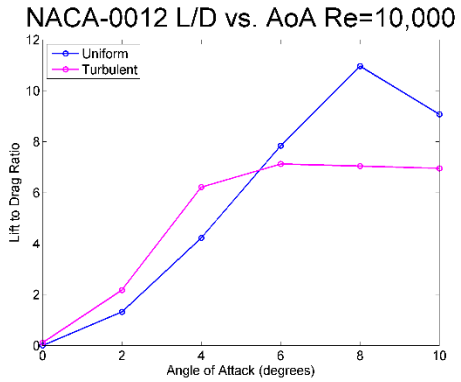

Figure 3.32 Lift to Drag Ratio vs. Angle of Attack for NACA-0012 Uniform (blue) and Turbulent (magenta) Cases.

3.3.3. Boundary Layer Statistics

Unlike the original flow regime results, it is necessary to look at the boundary layer statistics for more than just validation of the presence of and successful elimination of the AFL. For the new flow regime, the reason for the aerodynamic performance discrepancy could also be shown in the boundary layer statistics.

Figure 3.33 shows the instantaneous z-vorticity contour plots for cases with the AFL present. Immediately the differences between the previous flow regime and the new

are apparent. The boundary layer is significantly larger in the new simulations, with much larger vorticities present along the suction side of the airfoil. These figures show very clear flow separation along the suction side of the airfoil. It can be seen that the 8 degree uniform case shows signs of flow reattachment towards the trailing edge of the airfoil. The presence of this flow reattachment, which was the foundation of Ikeda's findings, could be the reason for the jump in lift shown in Figure 3.30. The turbulent contours show significant reduction in the separation region visible in the uniform cases.

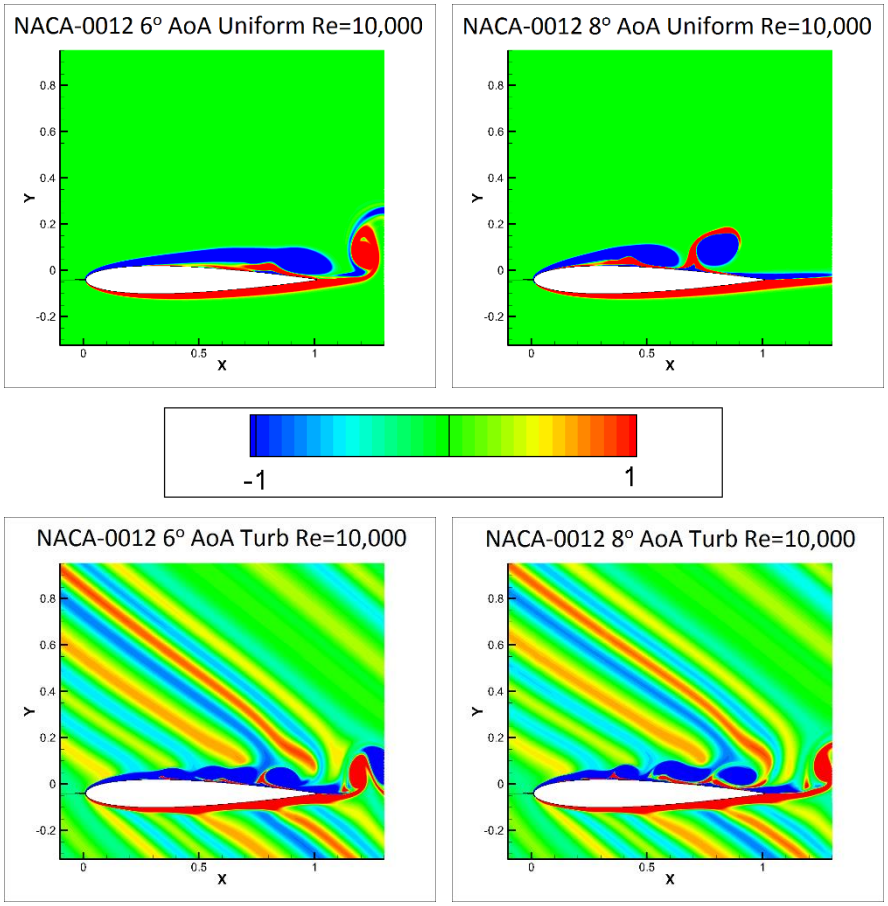

Figure 3.33 Instantaneous Z-Vorticity Contours for NACA-0012
Top) Uniform, Bottom) Turbulent Cases. Left) 6 ° AoA, Right) 8 ° AoA.

The presence of the separation region is also shown in the time-averaged U-velocity contours in Figure 3.34. The uniform contours show clear, large separation regions located close to the leading edge of the airfoil. It is shown in the 8 degree uniform

case that this separation region ends along the airfoil confirming that reattachment takes place near 90% chord. The turbulent cases show suppression of this separation region with small disturbances still present near the airfoil surface. Now that the flow reattachment has been confirmed as the catalyst for the jump in lift shown in Figure 3.30, the cause for the reattachment needs to be determined.

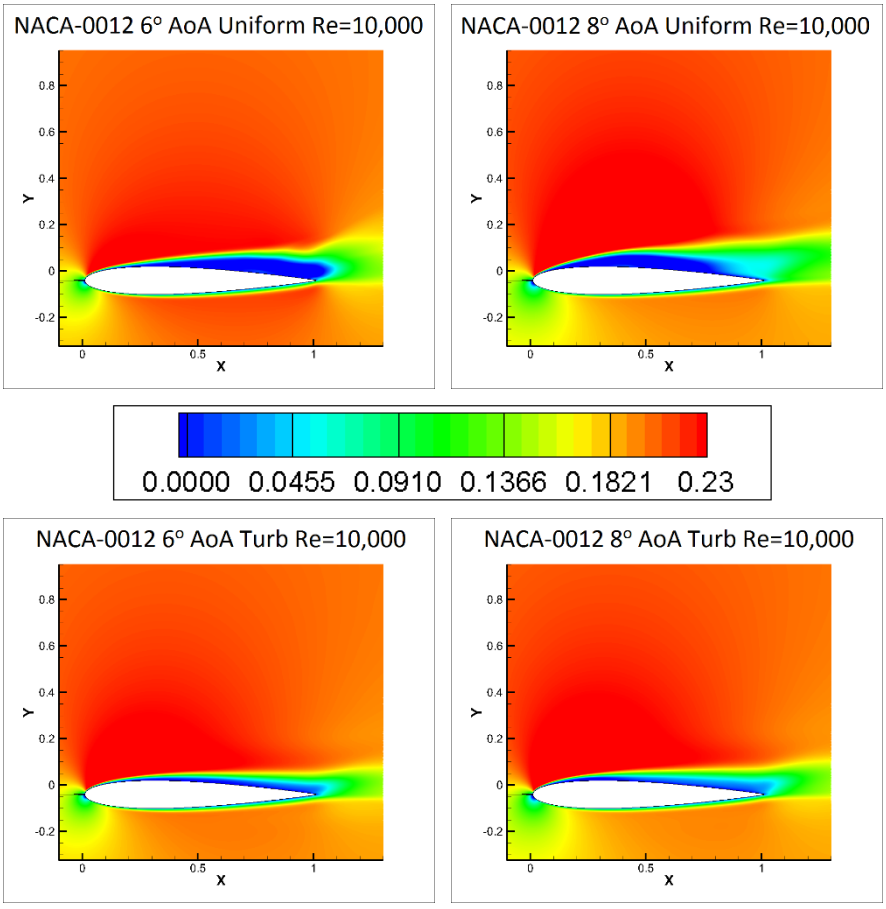

Figure 3.34 Time-averaged U-Velocity Contours NACA-0012
Top) Uniform, Bottom) Turbulent Cases. Left) 6 º AoA, Right) 8 º AoA.

The mean pressure coefficient plots in Figure 3.35 further confirm the presence of the separation region. Unlike the Re_c=140,000 cases shown earlier, there is significant pressure difference along the airfoil surface for both cases corresponding to differences in lift shown previously in Figure's 3.28 and 3.30. The hump shown in the uniform cases are both eliminated when upstream turbulence is introduced confirming the suppression

of AFL. The 8 degree case shows the presence of reattachment at the trailing edge especially compared to the 6 degree case where a significant difference can be seen between the uniform and turbulent case pressures along the trailing edge. Figure 3.36 shows the effect of the turbulence on the RMS pressure distribution. Similar to the earlier cases, the RMS pressure distribution shows significant peaks along the leading edge in the turbulent cases compared to the uniform cases. It also shows a consistent trend along the airfoil and trailing edge, dampening large peaks to a more consistent RMS pressure.

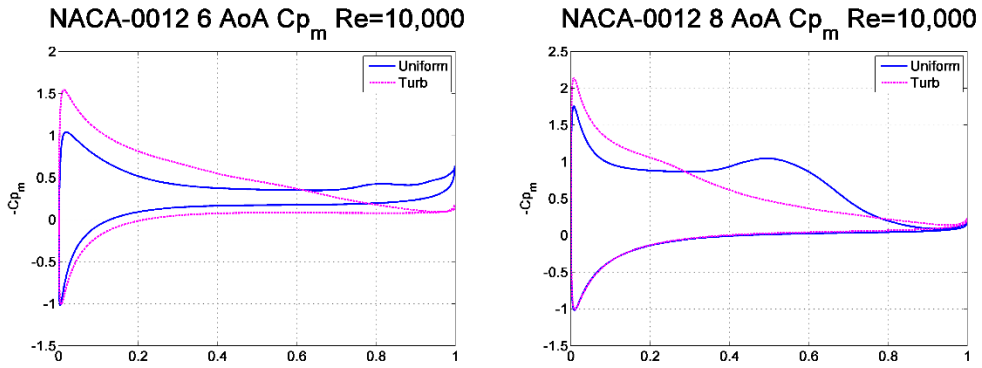

Figure 3.35 Mean Pressure Coefficient Comparison for NACA-0012 Uniform (blue) and Turbulent (magenta) Cases. Right) 6 º AoA, Left) 8 º AoA.

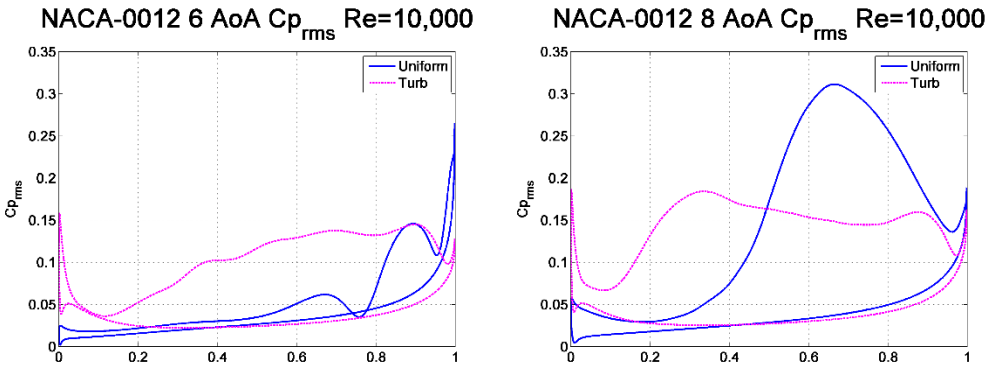

Figure 3.36 RMS Pressure Coefficient Comparison for NACA-0012. Uniform (blue) and Turbulent (magenta) Cases. Right) 6 º AoA, Left) 8 º AoA.

The Skin Friction Coefficient represented in Figure 3.37 yet again shows the separation region necessary for an AFL to be present as well as shows the reattachment region in the 8 degree case. The turbulent results show the suppression of this region

justifying the claim of the eliminated AFL.

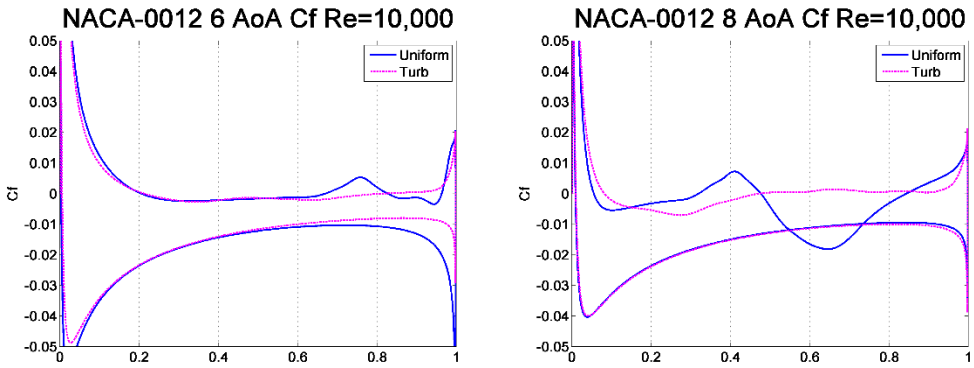

Figure 3.37 Skin Friction Coefficient Comparison for NACA-0012 Uniform (blue) and Turbulent (magenta) Cases. Right) 6 º AoA, Left) 8 º AoA.

3.4. SD7003: Mach 0.2 Re 10,000

The tested angles are shown in Table 3.4 and match the angles tested for the earlier flow regime. The angles where the AFL is present shows that the acoustic behavior of this flow is different than the previous flow regime. As with the NACA-0012 results, the SD7003 airfoil produced tones at higher angles of attack than found in the other test. The results for the lower angles (-2 through 4 degrees) did contain tones at certain angles but did not have the separation bubble necessary for the tones to be the result of an AFL. It was found that the tones produced at -4, 6 and 8 degrees AoA had both discrete tones in the acoustic spectra and clear evidence of the separation bubble required to produce the feedback loop.

Table 3.4 Geometric angle of attack investigated for SD7003 Re=10,000 Representative Cases (Bold)

Cases	AOA (degree)	Velocity (m/s)
Uniform	**-4,** -2, 0, 2, 4, **6, 8**	**69.4**
Turbulent	**-4,** -2, 0, 2, 4, **6, 8**	**69.4**

3.4.1. Pressure Spectra and Aerodynamic Performance

The surface pressure spectra plots in Figure 3.38 show the tones generated by the feedback loop in the uniform case as well as the scattering of the tones representative of the successful elimination of the AFL. The uniform cases show very minimal broadband noise, this was something also seen in the previous simulations of this airfoil at -2 degrees as well as the NACA-0012 at 6 degrees for this flow regime.

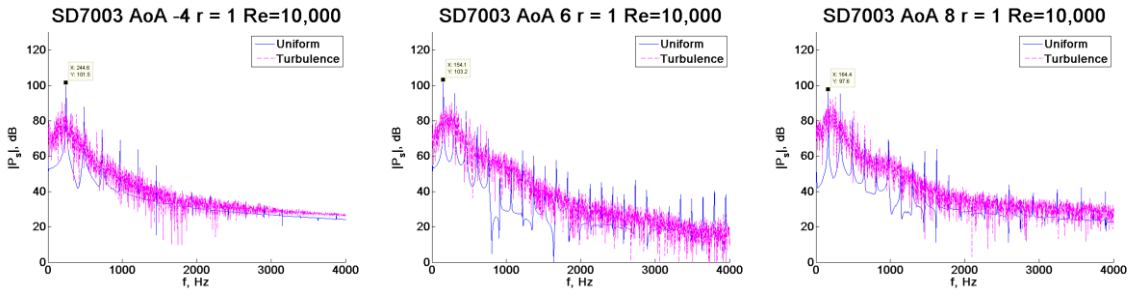

(a) (b) (c)

Figure 3.38 Acoustic Spectra Comparison of SD7003
Uniform (blue) and Turbulent (magenta) Cases. a) -4 º AoA, b) 6 º AoA, c) 8 º AoA.

The Lift Coefficient history plots shown in Figure 3.39 follow the trend of the symmetric NACA-0012 airfoil in this flow regime where the elimination of the AFL using turbulence shows a substantial change in the Lift at each AoA shown. With the cambered SD7003 airfoil, all three AoA with the AFL demonstrate the lift increase shown only in the 8 degree NACA-0012 simulation. Both the 6 and 8 degree case show flow reattachment in the boundary layer statistics plots in the following section, however, the -4 degree case does not show significant flow reattachment so there is currently no justification for the increase in lift for this case.

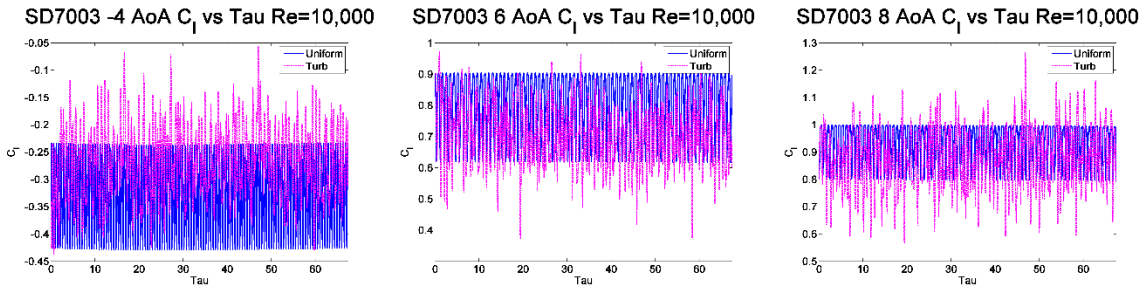

(a) (b) (c)

Figure 3.39 Coefficient of Lift vs. Non-Dimensional Time Comparison for SD7003 Uniform (blue) and Turbulent (magenta) Cases. a) -4 ^{o} AoA, b) 6 ^{o} AoA, c) 8 ^{o} AoA.

The FFT of the Lift history data shown in Figure 3.40 shows consistent peaks due to the tones generated by the feedback loop further validating the presence of the effect and the scattering accomplished by the upstream turbulence introduced in the flow.

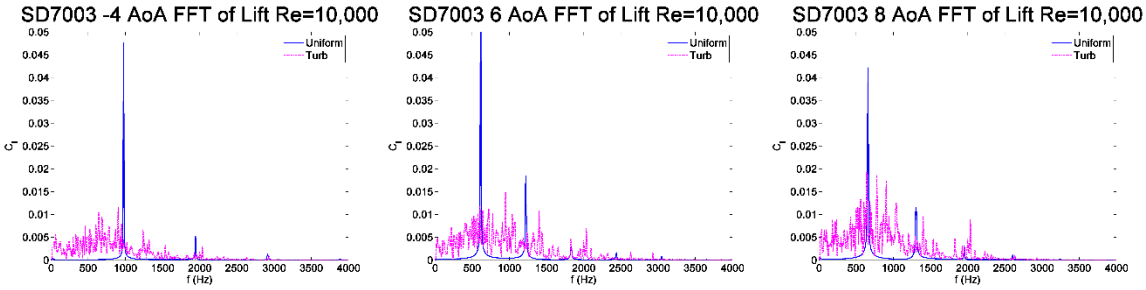

(a) (b) (c)

Figure 3.40 Comparison of Fast Fourier Transform of Lift for SD7003 Uniform (blue) and Turbulent (magenta) Cases. a) -4 ^{o} AoA, b) 6 ^{o} AoA, c) 8 ^{o} AoA.

The time-averaged lift coefficient for all simulated cases is compared to the theoretical flat-plate lift in Figure 3.41. The uniform and turbulent time-averaged lift plots show a consistent trend with the NACA-0012 results from Figure 3.30. For the SD7003 airfoil the transition occurs between 4 and 6 degrees AoA as opposed to the 6 and 8 degrees from the NACA-0012 airfoil. The transition in time-averaged lift plot corresponds to the presence of flow reattachment which is consistent with the results from the NACA-0012 simulations. The results are also compared to wind tunnel data from Selig et al., (1995) performed at Re_c=60,000. The results show a deviation between 0 and 4 degrees AoA when compared to the uniform flow simulation. While the

simulation and experiment are conducted at different Reynolds numbers, it is unlikely that the fairly small disparity in test conditions is responsible for such a large change in lift data. Without having access to boundary layer information and more complete pressure data it is not possible to determine the difference in results. The higher AoAs show consistent trends between the wind tunnel and uniform simulation. The time-averaged drag coefficient also follows a consistent trend when compared with the NACA-0012 where the turbulent cases show good correlation with the uniform cases at low AoA and have higher drag values at higher AoAs. The simulation results are compared against wind tunnel results from Selig et al., (1995). With a moderately lower Reynolds number than what was performed in the wind tunnel, the simulation results show substantial variation when compared to the wind tunnel results across all AoAs. Overall aerodynamic performance was analyzed using the lift to drag ratio in Figure 3.43. The lift to drag plots show that the presence of the AFL (-4, 6, and 8 degree cases) does correlate to an overall increase in aerodynamic performance consistent with Ikeda's findings.

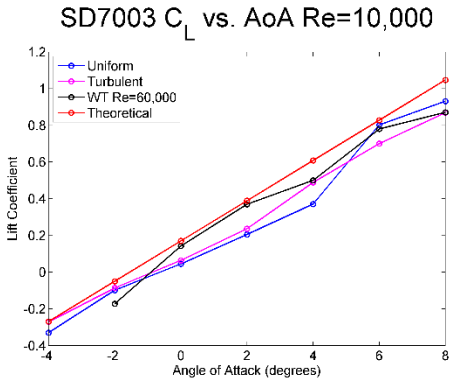

Figure 3.41 Time-averaged C_L vs. Angle of Attack Comparison for SD7003 Uniform (blue), Turbulent (magenta) Cases, Wind Tunnel Re=60,000 (black), Inviscid Flat-Plate (red).

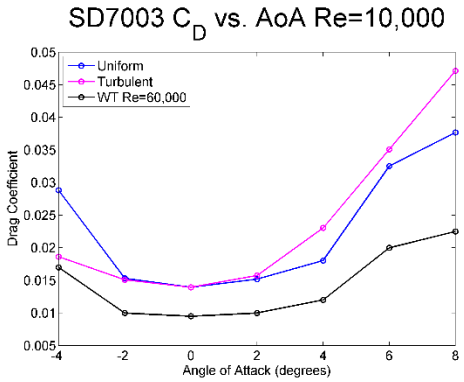

Figure 3.42 Time-averaged C_D vs. Angle of Attack Comparison for SD7003 Uniform (blue), Turbulent (magenta) Cases, Wind Tunnel Re=60,000 (black).

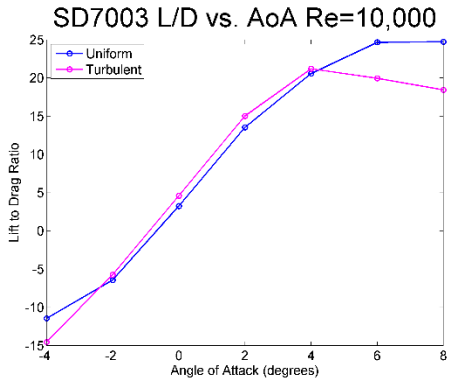

Figure 3.43 Lift to Drag Ratio vs. Angle of Attack for SD7003 Uniform (blue) and Turbulent (magenta) Cases.

3.4.3. Boundary Layer Statistics

The instantaneous z-vorticity for the SD7003 airfoil at -4, 6 and 8 degrees AoA are shown in Figure 3.44 for both uniform and turbulent simulations. The presence of large separation bubbles can be seen along the suction side of each angle of attack in the uniform cases. The turbulent results show the suppression of the separation bubble corresponding to the elimination of the AFL. The plots show the reattachment regions along the trailing edge for both the 6 and 8 degree uniform cases. The -4 degree case does not appear to achieve reattachment in the z-vorticity plot. The time-averaged U-velocity plots in Figure 3.45 validate the results shown in Figure 3.40. Here the reattachment

regions are visible for both the 6 and 8 degree cases with reattachment occurring earlier along the airfoil for the 8 degree case. The plots also confirm that the –4 case does not achieve flow reattachment along the airfoil. This validates the time-averaged lift coefficient results from Figure 3.41. Lift coefficient is consistently lower than the corresponding tripped boundary-layer case unless there is flow reattachment present regardless of the presence of the AFL. This is seen in the 6 and 8 degree NACA cases discussed in Section 3.3.

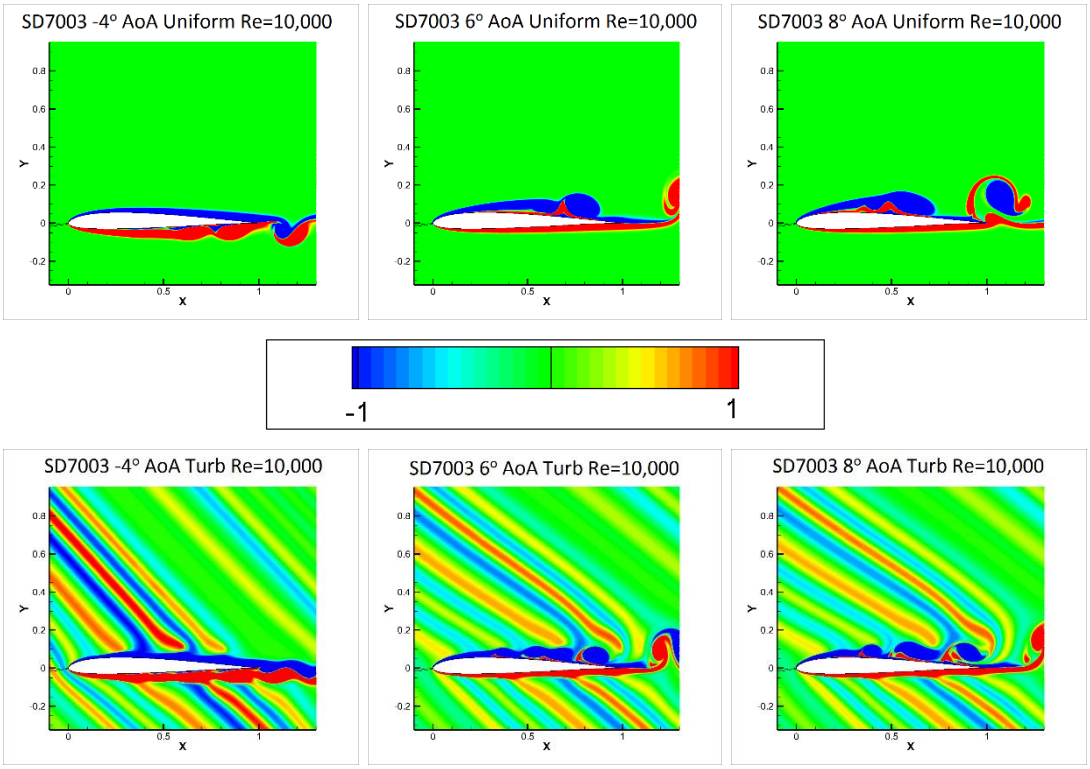

Figure 3.44 Instantaneous Z-Vorticity Contours of SD7003
Top) Uniform, Bottom) Turbulent Cases. Left) -4° AoA, Middle) 6° AoA, Right) 8° AoA.

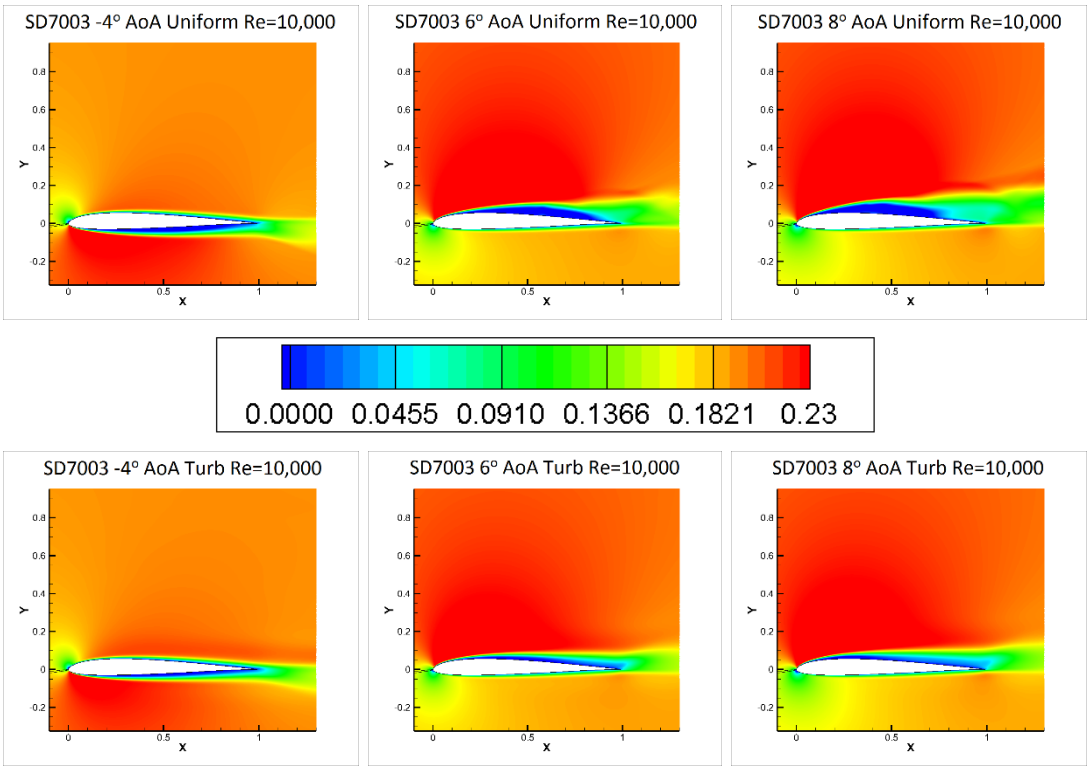

Figure 3.45 Time-averaged U-Velocity Contours for SD7003
Top) Uniform, Bottom) Turbulent Cases. Left) -4° AoA, Middle) 6° AoA, Right) 8° AoA.

The mean pressure coefficient, RMS pressure coefficient, and skin friction coefficient values along each airfoil are compared in Figures 3.46, 3.47, and 3.48 respectively. The humps present in the mean pressure coefficient plots in Figure 3.42 confirm the presence of the separation bubble that was visible in the z-vorticity and time-averaged U-velocity contour plots from Figure 3.44 and 3.45 respectively. The trailing edge section of the -4 degree case does show a dip that could correspond to flow reattachment explaining the negative lift increase observed. The RMS plots show that the turbulence introduced upstream reduced the large fluctuation peaks and created a more consistent variation along the airfoil surface. The skin friction plots show humps and dips corresponding to flow separation and attachment for the high angles of attack. The -4 degree case shows a hump along the suction side consistent with a separation bubble but does not appear to have the dip shown by the other plots. It appears to have a very

smooth transition from separated back to normal flow with the trailing edge of the uniform case matching well with the turbulent behavior.

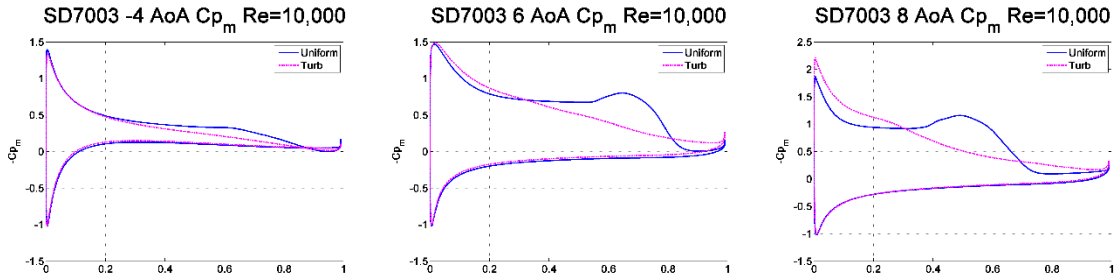

(a) (b) (c)

Figure 3.46 Mean Pressure Coefficient Comparison for SD7003 Uniform (blue) and Turbulent (magenta) Cases. a) -4 º AoA, b) 6 º AoA, c) 8 º AoA.

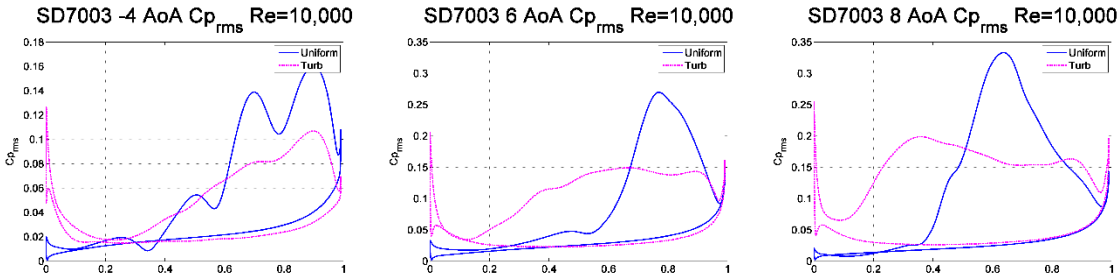

(a) (b) (c)

Figure 3.47 RMS Pressure Coefficient Comparison for SD7003 Uniform (blue) and Turbulent (magenta) Cases. a) -4 º AoA, b) 6 º AoA, c) 8 º AoA.

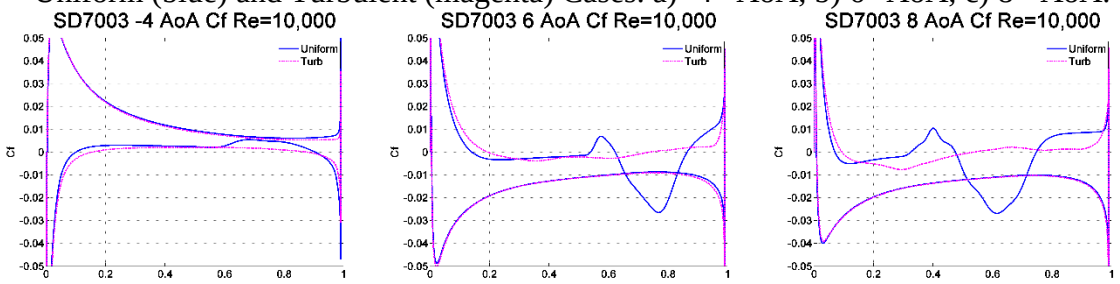

(a) (b) (c)

Figure 3.48 Skin Friction Coefficient Comparison for SD7003 Uniform (blue) and Turbulent (magenta) Cases. a) -4 º AoA, b) 6 º AoA, c) 8 º AoA.

4. Conclusion

High-accuracy 2D numerical simulations were conducted for the symmetric NACA-0012 and cambered SD7003 airfoils to investigate the effect of flow-acoustic resonant interactions on the airfoil aerodynamic performance. Each airfoil was tested at two flow regimes. The test conditions of the first flow were a fixed mean flow velocity of 16 m/s and Re_c=140,000. The next regime test conditions were a fixed mean flow velocity of 69.4 m/s and Re_c=10,000. For each regime the airfoils were tested at a wide range of AoAs to determine the angles where the AFL was present. Using a previously developed technique to impose upstream turbulence in numerical simulations, the airfoil aerodynamic responses were compared for uniform and turbulent upstream flow conditions. Results show the AFL to be present in the case of the uniform upstream flow condition and suppressed when turbulence with intensity of I=0.07 is introduced.

The first part of this study focused on results obtained for a symmetric NACA-0012 airfoil. Comparison of the pressure spectra for different inflow conditions revealed a dominant single peak tone for the uniform flow cases indicating the existence of the AFL, and a broadband hump for turbulent flow representative of the flow regimes with suppressed AFL. Boundary layer statistics were collected along the airfoil surface to illustrate the mechanism of the AFL suppression. Results indicate that the AFL occurrence coincided with the formation of the thin laminar separation zones sustained in the uniform flow cases. However, the existence or non-existence of such laminar separation zones did not entail any significant modifications in the mean pressure profiles, thus keeping the aerodynamic performance practically unchanged between the two flow regimes.

An additional study was conducted for a cambered SD7003 airfoil to include the effect of the airfoil geometry in the study. The boundary-layer was conducted for a cambered SD7003 airfoil, with both showing no significant impact due to the AFL on aerodynamic performance.

The results were found to be in disagreement with conclusions presented by Ikeda et al., (2014) who stated that the aerodynamic performance may be greatly affected by the existence of the AFL. It was proposed that the difference in findings could be a result of Ikeda focusing on a deep laminar flow regime with Re_c=10,000. Further investigation was performed at this flow regime in an attempt to reproduce the results.

The procedure from the initial simulations was followed for the new flow regime. The deep laminar flow had a strong effect on the aerodynamic performance with the uniform upstream flow cases showing significant dips and jumps throughout the AoA range tested. When upstream turbulence was introduced the lift curve behaved in a traditionally linear fashion but there were significant losses found throughout most AoA tested. There were noticeable jumps corresponding to flow reattachment observed throughout the boundary-layer statistics investigated for each case. This was expected due to the findings of Ikeda et al., (2014) but it did not allow for a definitive answer to be determined as to the cause of the flow reattachment. It has been argued that the presence of the AFL provides sufficient energy to excite the boundary-layer upstream in order to cause the flow to transition to turbulence sooner than natural. Because of the way these simulations are run, the boundary-layer is completely disrupted in the process making any meaningful comparison between cases with and without the AFL impossible. Further research was conducted into the effect of acoustic noise on the boundary-layer. In

research by Kurelek and Yarusevych (2016), they investigated the separation regions of airfoils without naturally occurring AFL's in a wind tunnel. They would then introduce tones consistent of those produced by an AFL, tones would be at a frequency matching the vortex shedding of the flow specified and speakers were positioned behind the airfoil, and would then compare the location of the separation and reattachment regions. Figure 4.1 is taken from this research and clearly shows the shift produced by the presence of acoustic tones. This result shows definitively that the presence of an AFL can cause the transition to turbulence to occur further upstream than without.

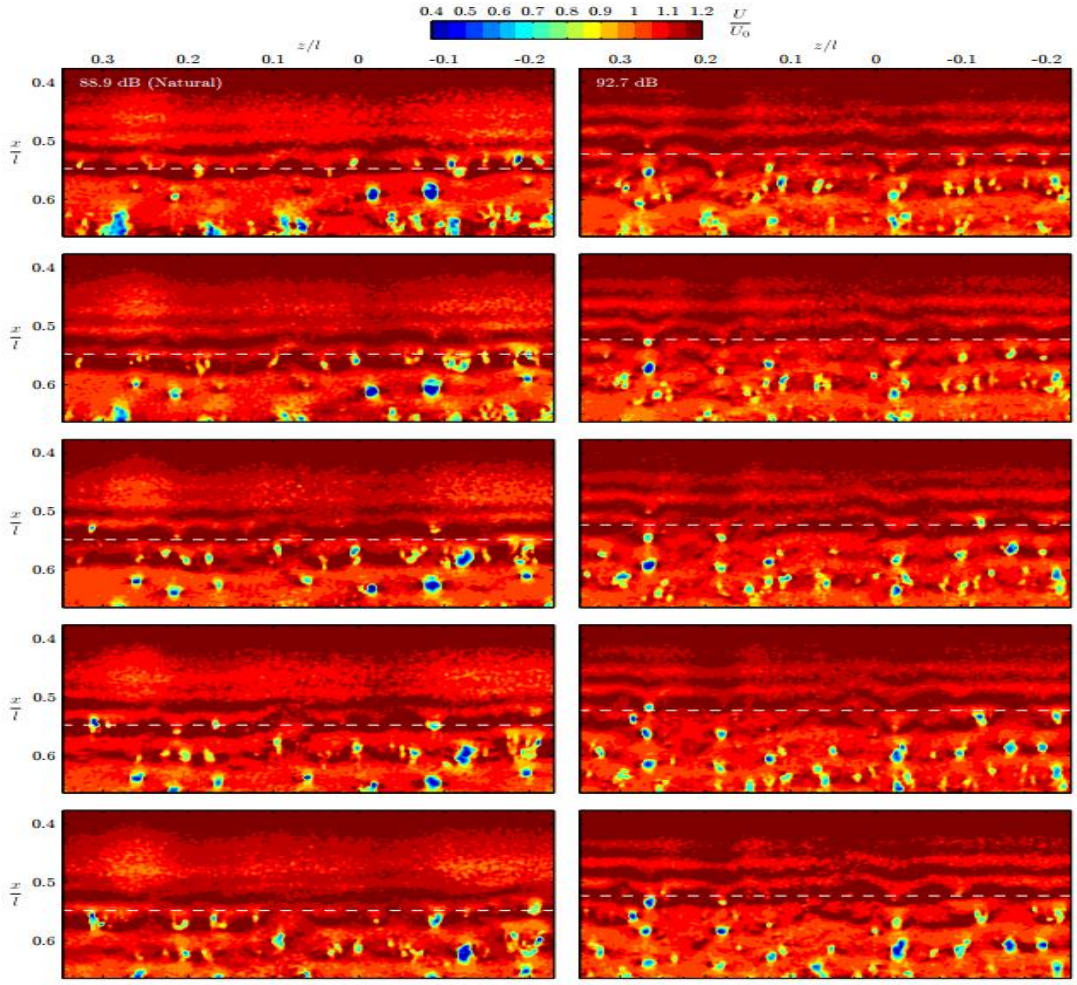

Figure 4.1 Instantaneous contours of streamwise velocity (Kurelek and Yarusevych 2016) Each consecutive frame is separated by $t^* = 2.5 \times 10^{-2}$. White dashed lines indicate mean reattachment points.

The purpose of this research was to determine if flow-acoustic resonant interactions effect aerodynamic performance of transitional airfoils. After conducting simulations on two different airfoils at two different flow regimes I believe it is possible to offer a definitive answer to this question. It is possible for tones produced by an AFL to alter the behavior of the boundary-layer upstream causing an early transition to turbulence, corresponding to earlier flow separation and sometimes allowing for reattachment that would not normally occur. If this effect allows for unnatural flow reattachment, it can provide increased aerodynamic performance in the form of increased lift. However, the presence of an AFL does not inherently improve performance. It has been shown that at higher Reynolds Numbers where the reattachment already occurs naturally, the airfoil performance is consistent with or without the AFL.

REFERENCES

Nash, E. C., Lowson, M. V., & McAlpine, A. (1999). Boundary-layer instability noise on aerofoils. Journal of Fluid Mechanics, vol. 382, pp. 27-61.

Ikeda, T., Fujimoto, D., Inasawa, A., Asai, M., (2014, January), "Unsteady Aerodynamic Characteristics of Cambered Four-digit NACA Airfoils at Low Reynolds Number", *AIAA Paper 2014-0049*, 52nd Aerospace Sciences Meeting, National Harbor.

Golubev, V., Nguyen, L., Mankbadi, R., Roger, M., and Visbal, M., (2014) "On flow-acoustic resonant interactions in transitional airfoils", *International Journal of Aeroacoustics*, vol. 13, pp. 1-38.

Golubev, V.V., Nguyen, L., Samsone, M., Hiner, W., Makbadi, R.R., Yakhina, G., Roger, M., (2015, June), "Parametric Investigations of Tonal Trailing-Edge Noise Generation by Moderate Reynolds Number Airfoils. Part II – Numerical Studies," *AIAA Paper 2015*, 15th AIAA Aviation Technology, Integration and Operation Conference, Dallas, Texas.

Visbal, M.R., Gaitonde, D.V., (2002), "On the Use of High-Order Finite-Difference Schemes on Curvilinear and Deforming Meshes". *J. Computational Physics*. vol. 181, pp. 155–185.

Anderson, D.A., Tannehill, J.C. and Pletcher, R.H., (1984), "Computational Fluid Mechanics and Heat Transfer". *McGraw-Hill Book Company*.

Visbal, M.R., Morgan, P.E. and Rizzetta, D.P., (2003) "An Implicit LES Approach Based on High-Order Compact Differencing and Filtering Schemes". *AIAA Paper 2003-4098*.

Lele, S.K., (1992), "Compact Finite Difference Schemes with Spectral-like Resolution". *J. Computational Physics*. vol. 103 pp. 16–42.

Beam, R. and Warming, R., (1978) "An Implicit factored scheme for the compressible Navier-Stokes equations". *AIAA J.* vol. 16(4), 393.

Kraichnan, R.H., (1970), Diffusion by a Random Velocity Field. *Physics of Fluids*, vol. 13, pp. 22-31.

Smirnov, R., Shi, S. and Celik, I., (2001), "Random Flow Generation Technique for Large

Eddy Simulations and Particle-Dynamics Modeling". *Journal of Fluids Engineering*, vol. 123, pp. 359-371.

Batten, P., Goldberg, U. and Chakravarthy, S., (2004) "Interfacing Statistical Turbulence Closures with Large-Eddy Simulation". *AIAA Journal*, vol. 42, No.3, pp. 485-492.

Golubev, V.V., Brodnick, J., Nguyen, L. and Visbal, M.R., (2001), "New Approach to Modeling Airfoil Interaction with Upstream Turbulence". *AIAA Paper* 2011-3899.

Golubev, V.V., Brodnick, J., Nguyen, L. and Visbal, M.R., (2012), "High-Fidelity Simulations of Airfoil Interaction with Upstream Turbulence", *AIAA Paper* 2012-3071.

Wagner, C., Huttl, T., Sagaut, P., (2007), "Large-Eddy Simulation for Acoustics", *Cambridge University Press*.

Desquesnes, M., Terracosl, M., Sagaut, P., (2007), "Numerical Investigation of the Tone Noise Mechanism over Laminar Airfoils", *J. Fluid Mechanics*. vol. 591, pp. 155-182.

Nguyen, L., Golubev, V.V., Mankbadi, R.R., Roger, M., Pasiliao, C., and Visbal, M.R., (2014, June), "Effect of Upstream Turbulence on Flow-Acoustic Resonance Interactions in Transitional Airfoils", *AIAA Paper 2014-3303*, 20^{h} AIAA/CEAS Aeroacoustics Conference, AIAA Aviation and Aeronautics Forum and Exposition, Atlanta.

Yakhina, G., Roger, M., Nguyen, L., and Golubev, V.V., (2015, June), "Parametric Investigations of Tonal Trailing-Edge Noise Generation by Moderate Reynolds Number Airfoils. Part I – Experimental Studies," *AIAA Paper 2015*, 15th AIAA Aviation Technology, Integration and Operation Conference, Dallas.

Galbraith, M., and Visbal, M.R., (2010, June), "Implicit Large Eddy Simulation of Low-Reynolds-Number Transitional Flow Past the SD7003 Airfoil", *AIAA Paper 2010-737*, 40th Fluid Dynamics Conference and Exhibit, Chicago, Illinois.

Sheldahl, R, E., Klimas, P, C., (1981, March), "Aerodynamic Characteristics of Seven Symmetrical Airfoil Sections Through 180-Degree Angle of Attack for Use in Aerodynamic Analysis of Vertical Axis Wind Turbines". Sandia National Laboratories, Albuquerque, New Mexico.

Selig, M. S., Donovan, J. F., and Fraser, D . B., (1989) "Airfoils at Low Speeds". H.A. Stokely, Virginia Beach, Virginia.

Selig, M. S., Guglielmo, J, J., Broeren, A. P., and Giguere, P., (1995), "Summary of Low-Speed Airfoil Data vol. 1", SoarTech Publications, Virginia Beach, Virginia.

Kurelek, J, W., Yarusevych, S., (2016, June), “The effect of acoustic excitation on the later stages of transition in a laminar separation bubble”, *AIAA paper 2016-3948,* 46th AIAA Fluid Dynamics Conference, Washington, D.C.